Solar Convection and Sunspots

Igor ROGACHEVSKII

Ben-Gurion University of the Negev, Beer Sheva, Israel

NORDITA, KTH Royal Institute of Technology and Stockholm University, Sweden

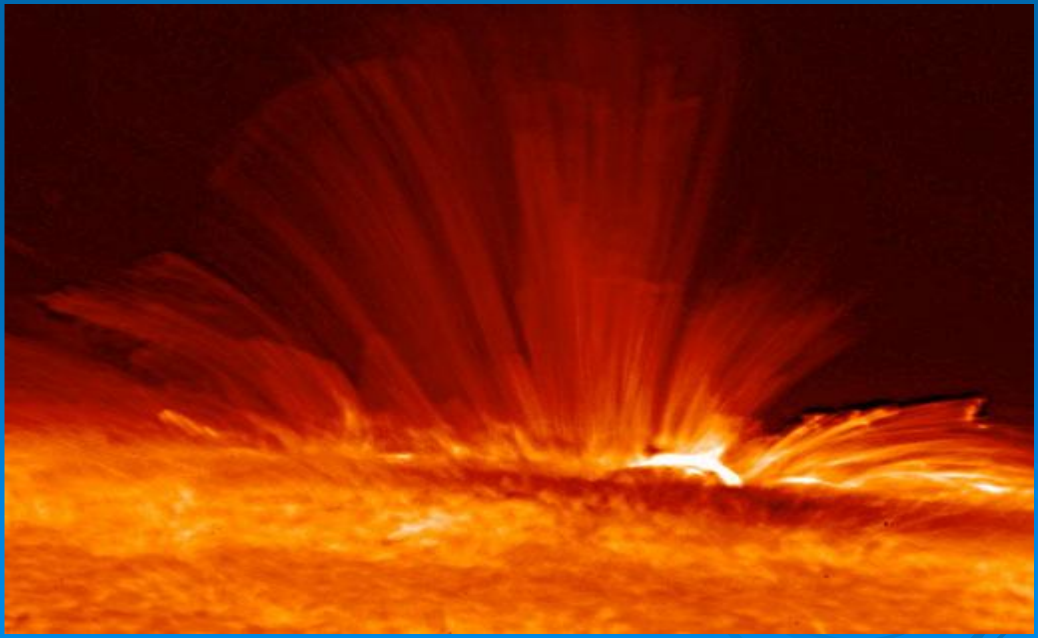

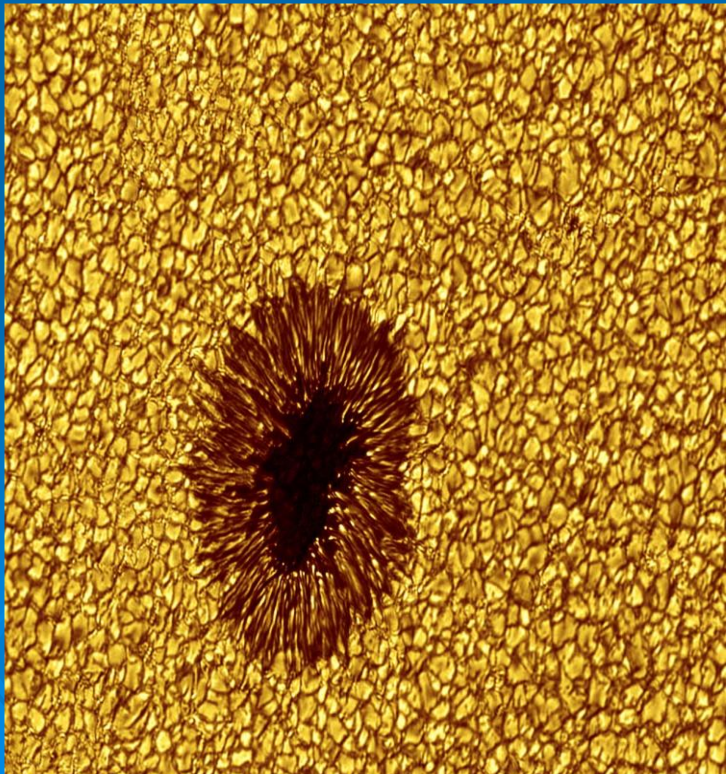

Sunspots and Solar Activity

- **What is the mechanism of formation of solar magnetic structures in turbulent convection zone?**
- **Solar dynamo mechanism can generate only weak (<< 1000G) nearly uniform large-scale magnetic field.**
- **How is it possible to create strongly inhomogeneous magnetic structures from originally uniform magnetic field?**

Theories of Sunspots Formation

1. Flux-Transport Dynamo

- 1). The solar dynamo produces strong magnetic fields at the bottom of the convection zone at the tachocline region (Parker 1975; Spiegel & Weiss 1980; Spiegel & Zahn 1992, Schou et al. 1998), where there is a strong shear layer, that produces strong toroidal magnetic field.
- 2) The field becomes unstable and rises upward in form of flux tubes, which reach the surface of the sun and form bipolar structures and sunspots (Caligari et al. 1995).

Criticism:

- A) However, the field in the tachocline region should be reach $10^5 G$, which is needed for a coherent flux tube to reach the surface without strong distortion (Choudhuri & Gilman 1987; D'Silva & Choudhuri 1993).
- B) The generation of such strong coherent magnetic flux tubes has not yet been seen in self-consistent dynamo simulations (Guerrero & Käpylä 2011; Nelson et al. 2011; Fan & Fang 2014).
- C) Helioseismology also does not support a deeply rooted flux tube scenario (Kosovichev & Stenflo 2008, Stenflo & Kosovichev 2012, Howe et al. 2009; Antia & Basu 2011).

2. Negative Effective Magnetic Pressure Instability (NEMPI)

Lorentz Force and Momentum Equation

$$\mathbf{J}\times\mathbf{B} = (\boldsymbol{\nabla}\times\mathbf{B})\times\mathbf{B} = -\boldsymbol{\nabla}\frac{\mathbf{B}^2}{2}+(\mathbf{B}\cdot\boldsymbol{\nabla})\mathbf{B} = -\nabla_j\left[\frac{1}{2}\boldsymbol{B}^2\delta_{ij} - B_iB_j\right]$$

$$\frac{\partial}{\partial t}\rho\,\mathbf{U}_i = -\nabla_j\,\Pi_{ij}$$

where

$$\Pi_{ij} = \rho\,U_iU_j + \delta_{ij}\,(p+\frac{1}{2}\mathbf{B}^2) - B_iB_j - \sigma^{\nu}_{ij}(\mathbf{U}) + \ldots$$

Averaged equation: $\mathbf{U} = \bar{\mathbf{U}} + \mathbf{u}\,,\qquad \mathbf{B} = \bar{\mathbf{B}} + \mathbf{b}$

$$\frac{\partial}{\partial t}\bar{\rho}\,\bar{\mathbf{U}}_i = -\nabla_j\,\bar{\Pi}_{ij}$$

where

$$\bar{\Pi}_{ij} = \bar{\rho}\,\bar{U}_i\bar{U}_j+\delta_{ij}\,(\bar{p}+\frac{1}{2}\bar{\mathbf{B}}^2)-\bar{B}_i\bar{B}_j-\bar{\sigma}^{\nu}_{ij}(\bar{\mathbf{U}})+\frac{1}{2}\langle\mathbf{b}^2\rangle\,\delta_{ij}-\langle b_ib_j\rangle+\bar{\rho}\langle u_iu_j\rangle+\ldots$$

DNS: The Result is Robust

$$\mathcal{P}_{\rm eff} = \frac{1}{2}(1 - q_p)\frac{\bar{\rm B}^2}{{\rm B}_{\rm eq}^2}$$

Effect does not exist only below $\mathrm{Rm} = 1$

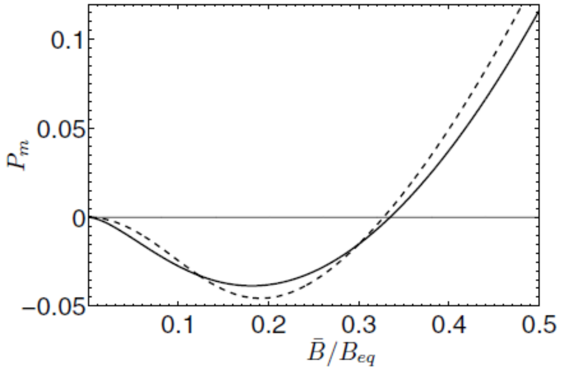

Fig. 3 The effective mean magnetic pressure $P_m(\overline{B}) = (1 - q_{\rm p})\overline{B}^2/\overline{B}_{\rm p}^2$ determined by Rogachevskii & Kleeorin (2007) – solid line, and by the model described by Eq. (26) – dashed line ($\overline{B}_{\rm p} = 0.21\, c_{\rm s0}\rho_0^{1/2}$ and $q_{\rm p0} = 4$).

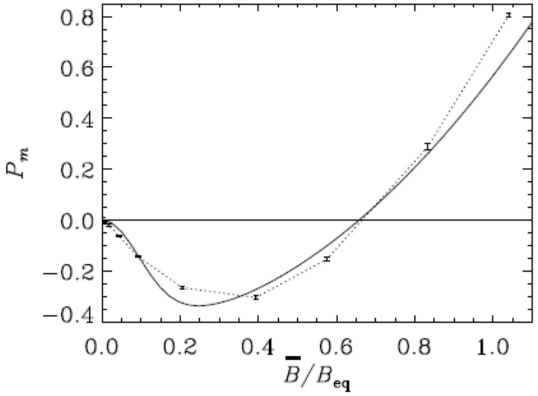

Fig. 4 Same as Fig. 3, but from simulation (dotted line). The solid line shows a fit [Eq. (26)] with $\overline{B}_{\rm p} = 0.022\, c_{\rm s0}\rho_0^{1/2}$ (corresponding to $\overline{B}_{\rm p}/B_{\rm eq} = 0.18$) and $q_{\rm p0} = 21$.

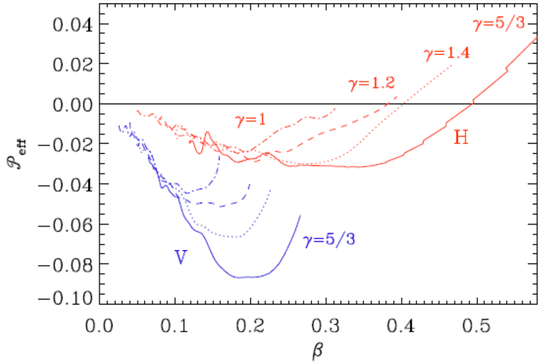

Fig. 7. Effective magnetic pressure obtained from DNS in a polytropic layer with different γ for horizontal (H, red curves) and vertical (V, blue curves) mean magnetic fields.

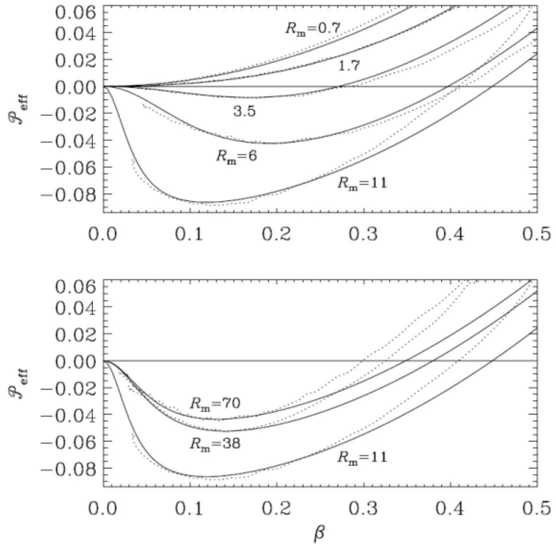

Figure 7. Normalized effective magnetic pressure, $\mathcal{P}_{\rm eff}(\beta)$, for low (upper panel) and higher (lower panel) values of Re_M. The solid lines represent the fits to the data shown as dotted lines.

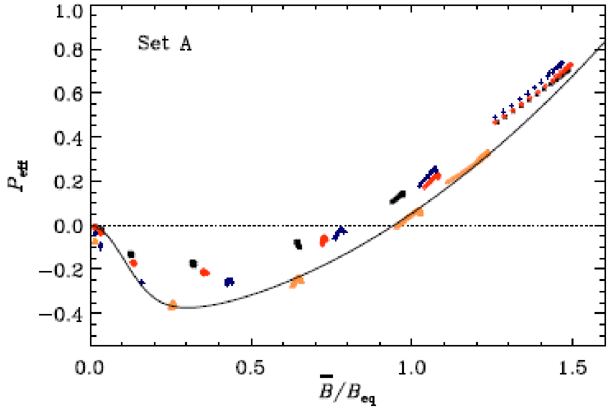

Figure 2. Effective magnetic pressure as a function of the mean magnetic field from weakly stratified Runs A1–A29 with an imposed horizontal field $\boldsymbol{B}_0 = B_0\hat{\boldsymbol{x}}$. The black stars, red diamonds, blue crosses, and yellow triangles denote simulations with Rm $\approx$ 10, 20, 50, and 70, respectively. We omit points near the boundaries at $z/d < 0.35$ and $z/d > 0.65$. The dashed and dotted lines correspond to approximate fits determined by Eq. (30), with $q_{\rm p0} = 35$ and $B_{\rm p} = 0.2B_{\rm eq}$, respectively.

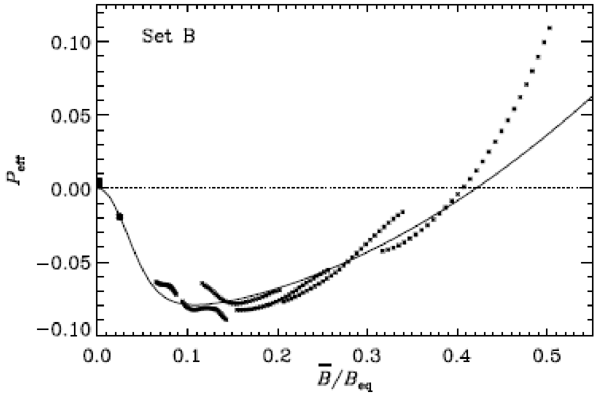

Figure 3. Same as Figure 2 but for Runs B1–B8 for Rm $=$ 40–50. The solid line corresponds to a fit with $q_{\rm p0} = 70$ and $B_{\rm p} = 0.063B_{\rm eq}$

Equation of State for Isotropic Turbulence

N. Kleeorin, I. Rogachevskii and A. Ruzmaikin,
Sov. Astron. Lett. 15, 274-277 (1989); Sov. Phys. JETP 70, 878-883 (1990)

N. Kleeorin and I. Rogachevskii, *Phys. Rev. E 50, 2716-2730 (1994)*

I. Rogachevskii and N. Kleeorin, *Phys. Rev. E 76, 056307 (2007)*

The total turbulent pressure is reduced when magnetic fluctuations are generated

The equation of state for an isotropic turbulence

$$p_T = \frac{1}{3} W_m + \frac{2}{3} W_k \; ,$$

where p_T is the total (hydrodynamic plus magnetic) turbulent pressure,

$W_m = \langle \mathbf{b}^2 \rangle / 2\mu$ is the energy density of the magnetic fluctuations,

$W_k = \rho_0 \langle \mathbf{u}^2 \rangle / 2$ is the kinetic energy density.

Total Turbulent Energy

The total energy density W_T of the homogeneous turbulence with a nonzero uniform mean magnetic field is conserved

$$\mathrm{W_k + W_m = const.}$$

The uniform large-scale magnetic field performs no work on the turbulence. It can only redistribute the energy between hydrodynamic fluctuations and magnetic fluctuations.

The total energy density $\mathrm{W_T = W_k + W_m}$ of the homogeneous turbulence with a mean magnetic field $\bar{\mathrm{B}}$

$$\frac{\partial W_T}{\partial t} = I_T - \frac{W_T}{\tau_0} + \eta_T \frac{(\boldsymbol{\nabla} \times \bar{\mathrm{B}})^2}{\mu}$$

$I_T =$ is the energy source of turbulence,

W_T/τ_0 determines the dissipation of the turbulent energy.

Strong reduction of Turbulent Pressure

Combining the equations:

$$p_T = \frac{1}{3}W_m + \frac{2}{3}W_k = \frac{2}{3}(W_k + W_m) - \frac{1}{3}\mathrm{W_m} , \qquad \mathrm{W_k + W_m = const} ,$$

we can express the change of turbulent pressure δp_T in terms of the change of the magnetic energy density δW_m

$$\delta \mathrm{p_T} = -\frac{1}{3}\delta \mathrm{W_m}$$

Therefore, the turbulent pressure is reduced when magnetic fluctuations are generated (i.e., $\delta \mathrm{W_m} > 0$).

Equation of State for Anisotropic Turbulence

The equation of state for an anisotropic turbulence

$$p_T = \frac{1}{3(1+\sigma/2)} W_m + \frac{2}{3}\left(\frac{1+3\sigma/4}{1+\sigma/2}\right) W_k \; ,$$

where $0 \leq \sigma < \infty$ is the degree of anisotropy of turbulence.

For a two-dimensional turbulence: $\sigma \to \infty$ and the equation of state reads:

$$p_T = \frac{2}{3\sigma} W_m + W_k = (W_k + W_m) - \mathbf{W_m} \; ,$$

Thus, the change of turbulent pressure δp_T for the two-dimensional turbulence is

$$\delta \mathbf{p_T} = -\delta \mathbf{W_m}$$

Magnetic Fluctuations and Turbulent Pressure

The total turbulent pressure is decreased also by the tangling of the large-scale mean magnetic field $\bar{\mathrm{B}}$ by the velocity fluctuations.

$$\langle \mathrm{b}^2 \rangle = \langle \mathrm{b}^2 \rangle^{(0)} + a_m(\bar{B}, \mathrm{Rm}) \bar{\mathrm{B}}^2 + \dots ,$$

where $\langle \mathrm{b}^2 \rangle^{(0)}$ determines the magnetic fluctuations due to a small-scale dynamo.

The total turbulent pressure reads

$$p_T = p_T^{(0)} - q_p \frac{\bar{\mathrm{B}}^2}{2\mu} , \qquad q_p = \left(\frac{1}{3} \div 1\right) a_m(\bar{B}, \mathrm{Rm}) .$$

The sign of a_m (and q_p) is positive when magnetic fluctuations are generated and negative when they are damped.

Effective Magnetic Pressure

The total pressure is

$$p_{tot} = p_k + p_T + P_B(\bar{B}) \ ,$$

where p_k is the fluid pressure and $P_B(\bar{B}) = \frac{\bar{\mathrm{B}}^2}{2\mu}$ is the magnetic pressure of the mean field.

Now we examine the part in p_{tot} that depends on the mean (large-scale) magnetic field $\bar{\mathrm{B}}$:

$$\mathrm{P_m}(\bar{\mathrm{B}}) = P_B(\bar{B}) - \mathrm{q_p}(\bar{\mathrm{B}})\frac{\bar{\mathrm{B}}^2}{2\mu} = (1 - \mathrm{q_p}(\bar{\mathrm{B}}))\frac{\bar{\mathrm{B}}^2}{2\mu} \equiv Q_p(\bar{B})\frac{\bar{\mathrm{B}}^2}{2\mu} \ ,$$

$$p_{\mathrm{tot}} = p + \mathrm{P_m}(\bar{\mathrm{B}}) = p + \mathrm{Q_p}(\bar{\mathrm{B}})\frac{\bar{\mathrm{B}}^2}{2\mu} \ ,$$

where $p = p_k + p_T^{(0)}$. The pressure $P_m(\bar{B})$ is the combined mean magnetic pressure.

Methods and Approximations

- **Quasi-Linear Approach** or Second-Order Correlation Approximation (SOCA) or First-Order Smoothing Approximation (FOSA)

  Rm << 1 , Re << 1

  Steenbeck, Krause, Rädler (1966); Roberts, Soward (1975)

- **Tau-approaches** (spectral tau-approximation) – **third-order or high-order closure**

  Re >> 1 and Rm >> 1

  Orszak (1970); Pouquet, Frisch, Leorat (1976);
  Kleeorin, Rogachevskii, Ruzmaikin (1990); Rogachevskii, Kleeorin (2007)

- **Renormalization Procedure** (renormalization of viscosity, diffusion, electromotive force and other turbulent transport coefficients) - **Re >> 1 and Rm >> 1 , there is no separation of scales.**

  Moffatt (1981; 1983);
  Kleeorin, Rogachevskii (1994)

DNS: The Result is Robust

$$\mathcal{P}_{\rm eff} = \frac{1}{2}(1 - q_p)\frac{\bar{\rm B}^2}{{\rm B}_{\rm eq}^2}$$

Effect does not exist only below $\mathrm{Rm} = 1$

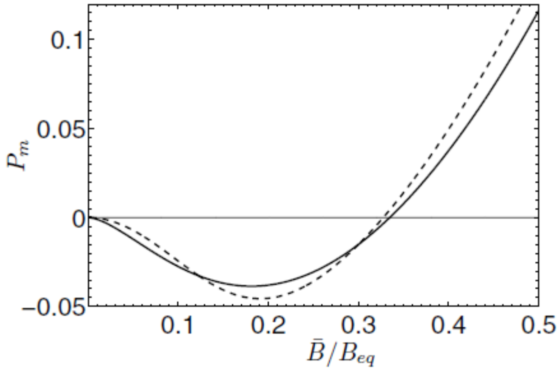

Fig. 3 The effective mean magnetic pressure $P_m(\overline{B}) = (1 - q_{\rm p})\overline{B}^2/\overline{B}_{\rm p}^2$ determined by Rogachevskii & Kleeorin (2007) – solid line, and by the model described by Eq. (26) – dashed line ($\overline{B}_{\rm p} = 0.21\, c_{\rm s0}\rho_0^{1/2}$ and $q_{\rm p0} = 4$).

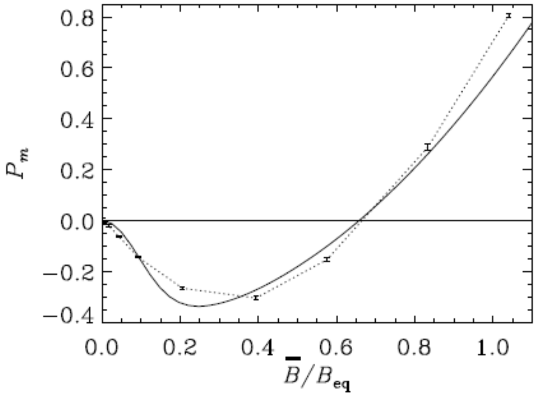

Fig. 4 Same as Fig. 3, but from simulation (dotted line). The solid line shows a fit [Eq. (26)] with $\overline{B}_{\rm p} = 0.022\, c_{\rm s0}\rho_0^{1/2}$ (corresponding to $\overline{B}_{\rm p}/B_{\rm eq} = 0.18$) and $q_{\rm p0} = 21$.

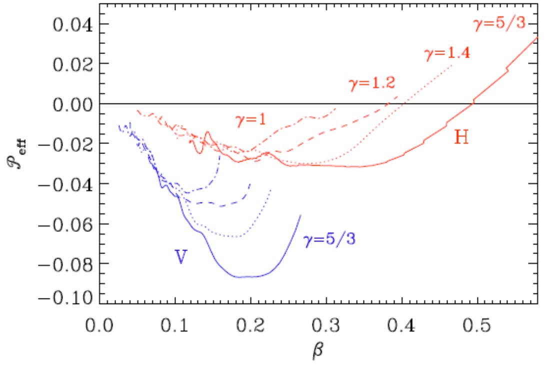

Fig. 7. Effective magnetic pressure obtained from DNS in a polytropic layer with different γ for horizontal (H, red curves) and vertical (V, blue curves) mean magnetic fields.

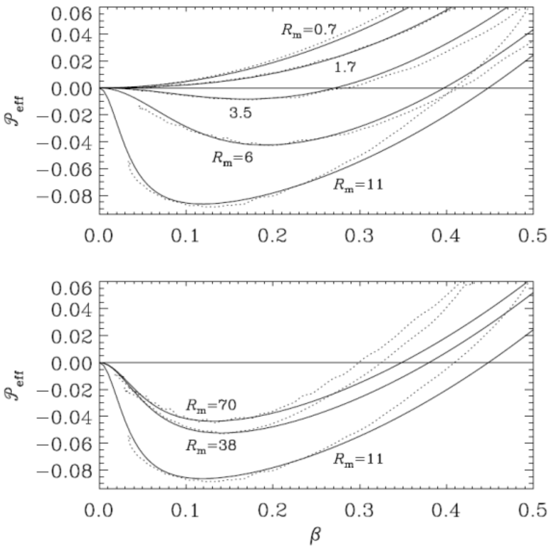

Figure 7. Normalized effective magnetic pressure, $\mathcal{P}_{\rm eff}(\beta)$, for low (upper panel) and higher (lower panel) values of Re_M. The solid lines represent the fits to the data shown as dotted lines.

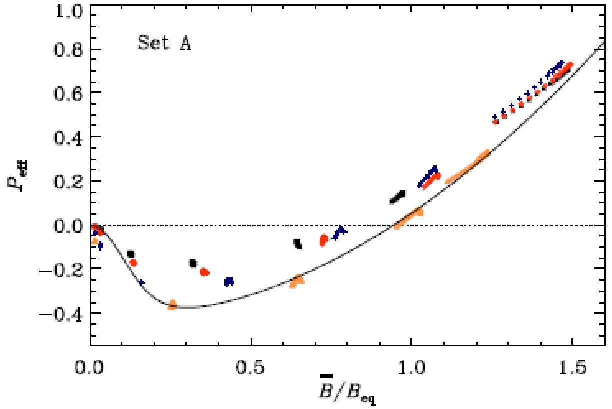

Figure 2. Effective magnetic pressure as a function of the mean magnetic field from weakly stratified Runs A1–A29 with an imposed horizontal field $\boldsymbol{B}_0 = B_0\hat{\boldsymbol{x}}$. The black stars, red diamonds, blue crosses, and yellow triangles denote simulations with $\mathrm{Rm} \approx 10$, 20, 50, and 70, respectively. We omit points near the boundaries at $z/d < 0.35$ and $z/d > 0.65$. The dashed and dotted lines correspond to approximate fits determined by Eq. (30), with $q_{p0} = 35$ and $B_p = 0.2B_{\rm eq}$, respectively.

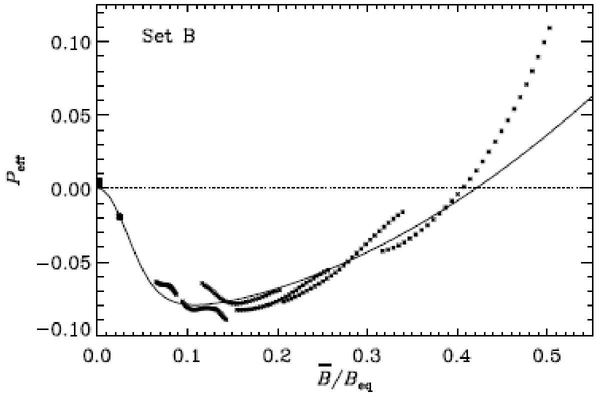

Figure 3. Same as Figure 2 but for Runs B1–B8 for $\mathrm{Rm} = 40$–50. The solid line corresponds to a fit with $q_{p0} = 70$ and $B_p = 0.063B_{\rm eq}$

Large-Scale MHD-Instability

Let us estimate the growth rate of this instability. Neglecting dissipative processes for simplicity's sake, we shall retain only the Archimedes force in the momentum equation of the magnetic flux tube

$$\frac{d^2\zeta}{dt^2} = -\left(\frac{C_A}{C_s}\right)^2 \frac{gQ_p(L_B - L_\rho)}{L_B L_\rho}\zeta \ ,$$

where $C_A = \bar{B}a/\sqrt{\mu\rho a}$ is the Alfven velocity. The growth rate of this instability is given by

$$\gamma \simeq \frac{C_A}{L_\rho}\left[Q_p\left(\frac{L_\rho}{L_B} - 1\right)\right]^{1/2} \ .$$

Here $L_\rho \simeq C_s^2/g$.

Large-Scale MHD-Instability (NEMPI)

A. Brandenburg, K. Kemel, N. Kleeorin, Dh. Mitra, and I. Rogachevskii, Astrophys. J. Lett. 740, L50 (2011); Solar Phys. 280, 321-333 (2012).

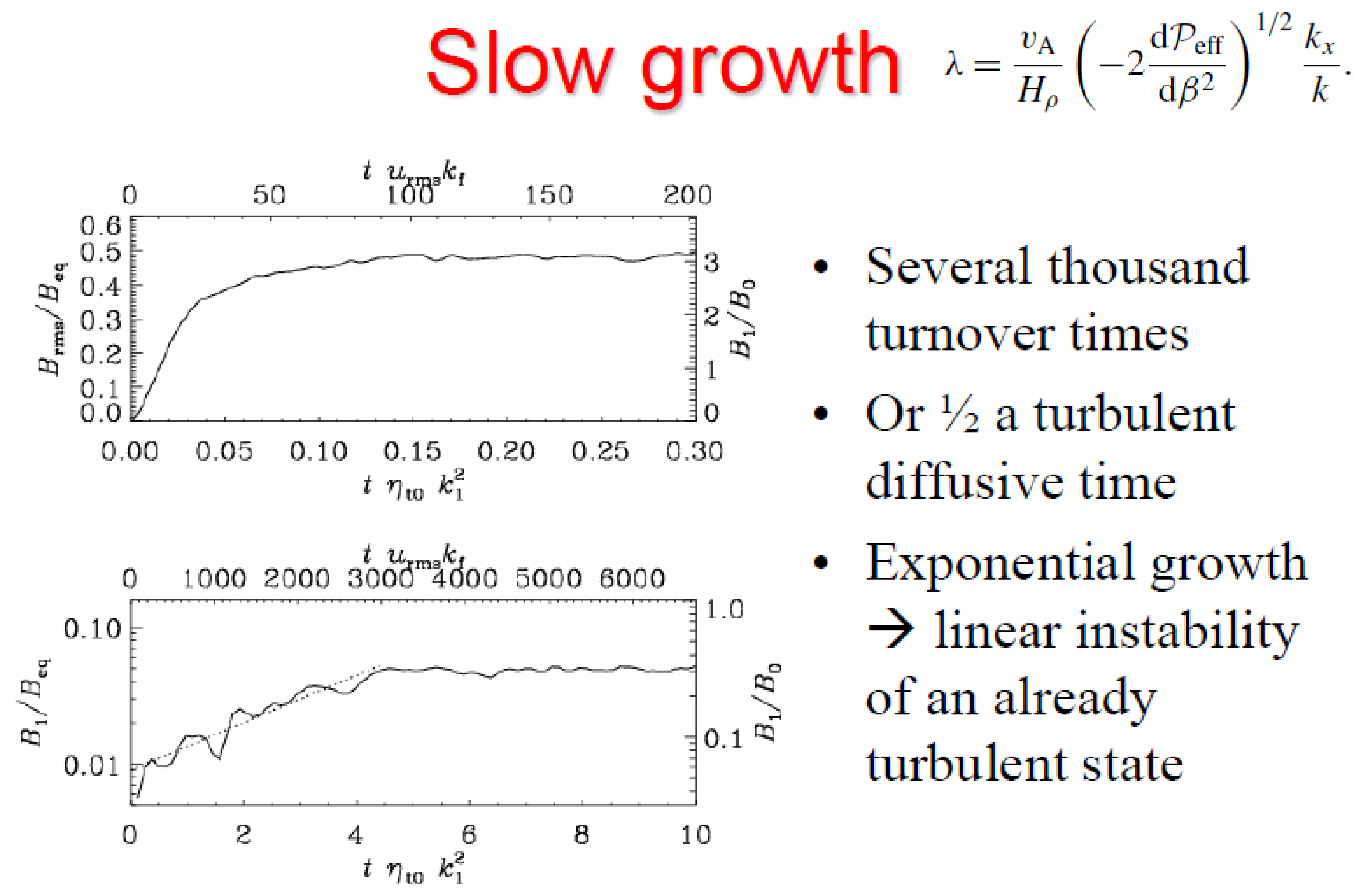

Slow growth

$$\lambda = \frac{v_{\rm A}}{H_\rho}\left(-2\frac{{\rm d}\mathcal{P}_{\rm eff}}{{\rm d}\beta^2}\right)^{1/2}\frac{k_x}{k}.$$

- Several thousand turnover times
- Or ½ a turbulent diffusive time
- Exponential growth → linear instability of an already turbulent state

NEMPI is the Large-Scale Instability

A. Brandenburg, O. Gressel, S. Jabbari, N. Kleeorin, I. Rogachevskii,
Astron. Astrophys. 562, A53 (2014).

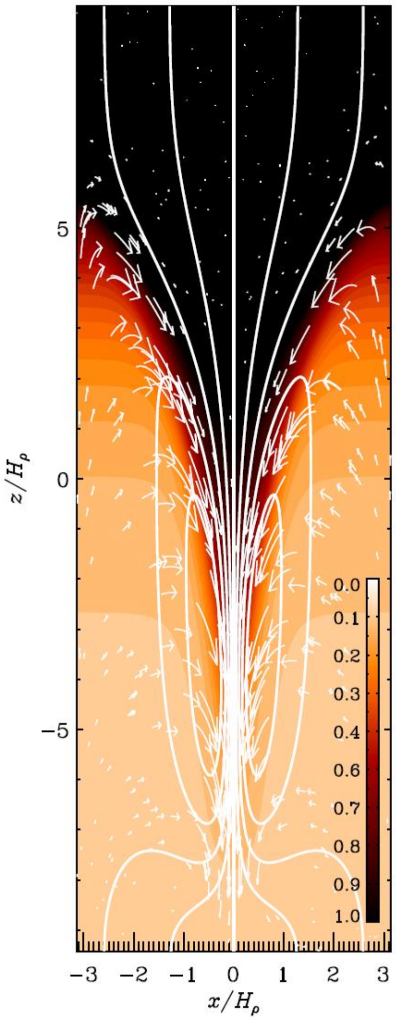

Fig. 5. $\overline{B}_z/B_{\rm eq}$ together with field lines and flow vectors from MFS, for Run Bv05/33 with $B_0/B_{\rm eq0} = 0.05$. The flow speed varies from $-0.27u_{\rm rms}$ (downward) to $0.08u_{\rm rms}$ (upward).

1. A local increase of the magnetic field causes a decrease of the negative effective magnetic pressure.
2. This is compensated for by enhanced gas pressure, leading to enhanced gas density, so the gas is heavier than its surroundings and sinks.
3. This results in a positive feedback loop: downflow compresses the magnetic field, the effective magnetic pressure becomes more negative, gas pressure increases, so the density increases, and the downflow accelerates, and causes NEMPI.

$$P_{\rm tot} = \rho T + (1 - q_p)\frac{\overline{\mathbf{B}}^2}{2}$$

Formation and Destruction of Bipolar Magnetic Structures

J. Warnecke, I.R. Losada, A. Brandenburg, N. Kleeorin and I. Rogachevskii,
Astrophys. J. Lett., 777, L37 (2013); Astron. Astrophys., 589, A125 (2016).

Imposed horizontal field.

$$k_f = 30\,k_1;$$

512 x 512 x 1024; 1024^3

BOUNDARY CONDITIONS
at the top and bottom:

$$U_z = 0, \quad \nabla_z U_x = \nabla_z U_y = 0$$

But

$$z = -\pi :$$

$$B_z = 0, \quad \nabla_z B_x = \nabla_z B_y = 0$$

$$z = 2\pi :$$

$$B_x = B_y = 0.$$

Re=40, $\mathrm{Pr}_M = 0.06 - 1$

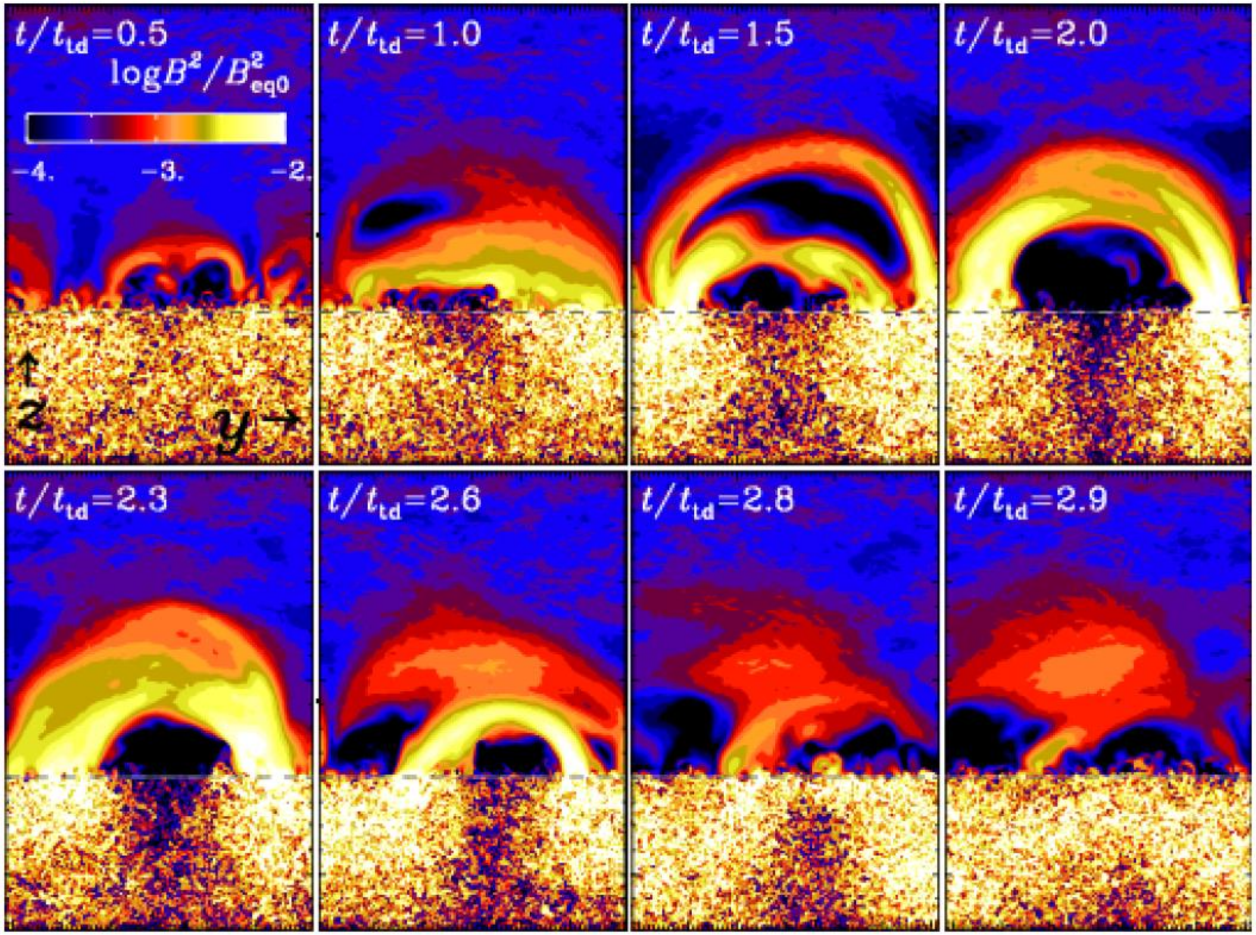

FIG. 5.— Time series of B^2/B^2_{eq0} in a vertical cut through the bipolar region at $x = 0$. Note the y axis is shifted the see the formation of the loop.

Formation and Destruction of Bipolar Magnetic Structures

J. Warnecke, I.R. Losada, A. Brandenburg, N. Kleeorin and I. Rogachevskii,

Astrophys. J. Lett., 777, L37 (2013); Astron. Astrophys., 589, A125 (2016).

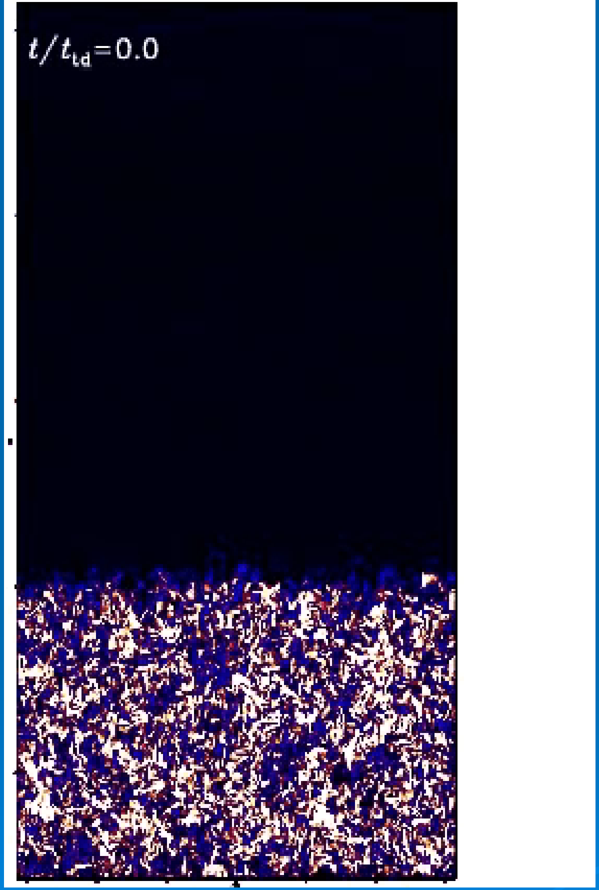

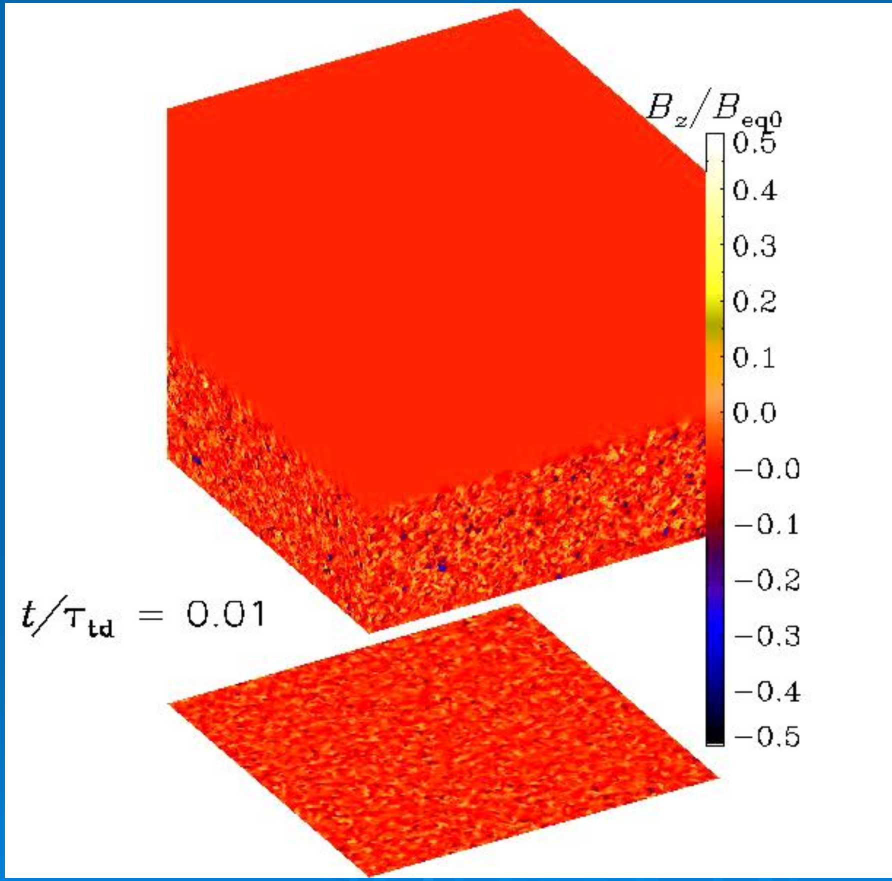

Magnetic Structures

J. Warnecke, I.R. Losada, A. Brandenburg, N. Kleeorin and I. Rogachevskii,
Astrophys. J. Lett., 777, L37 (2013), Astron. Astrophys., 589, A125 (2016).

Simulations

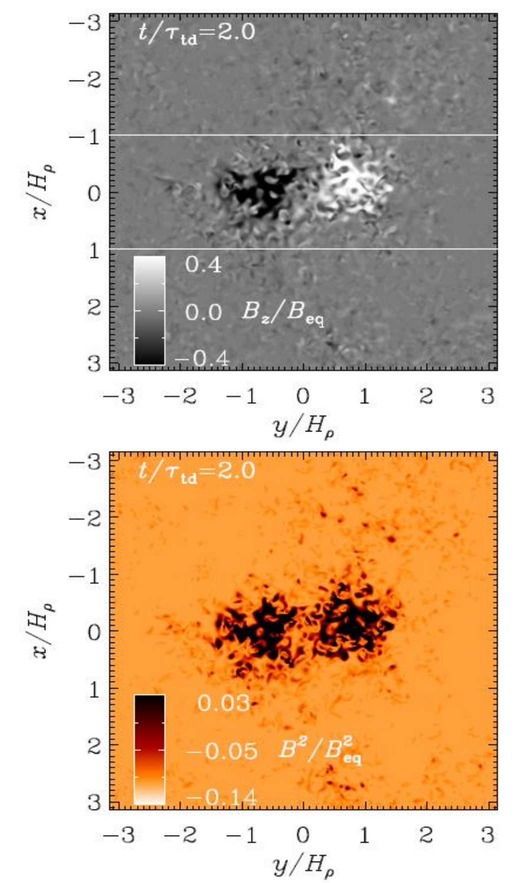

FIG. 1.— *Upper panel:* normalized vertical magnetic field $B_z/B_{\rm eq}$ of the bipolar region at the surface ($z = 0$) of the simulation domain. The white lines delineate the area shown in Figure 3. *Lower panel:* normalized magnetic energy $B^2/B^2_{\rm eq}$ of the two regions relative to the rest of the surface. Note that we clip both color tables to increase the visualization of the structure. The field strength reaches around $B_z/B_{\rm eq} = 1.4$.

Sunspots

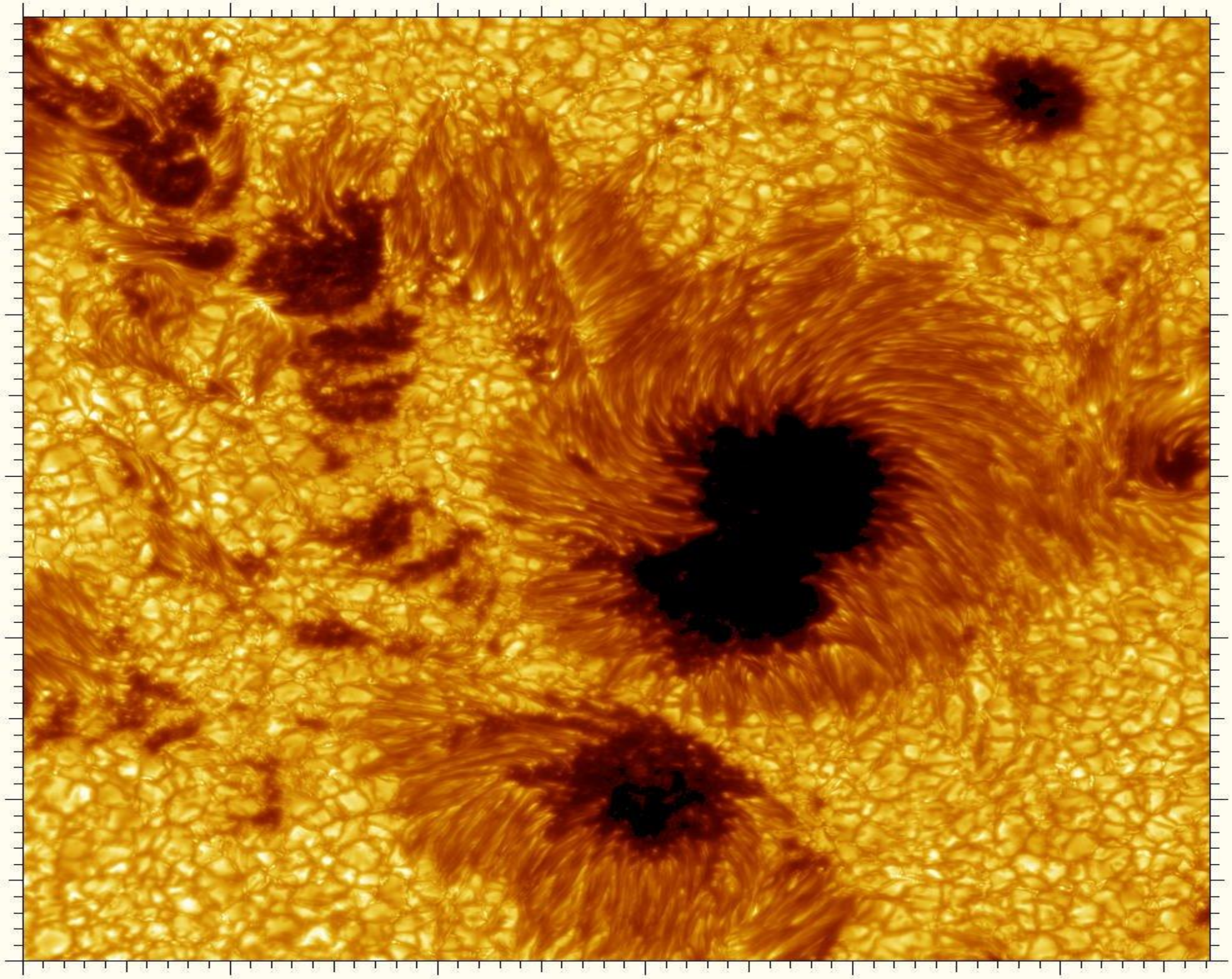

Formation of Magnetic Spots in DNS

Brandenburg, Kleeorin, Rogachevskii, ApJL 776, L23 (2013)

$$256^3; 512^3; \; 1024^3$$

PENCIL CODE

$$k_f = 30\, k_1; \qquad \mathrm{Rm} = \frac{u_{rms}}{\eta\, k_f} = 18; 40; 95$$

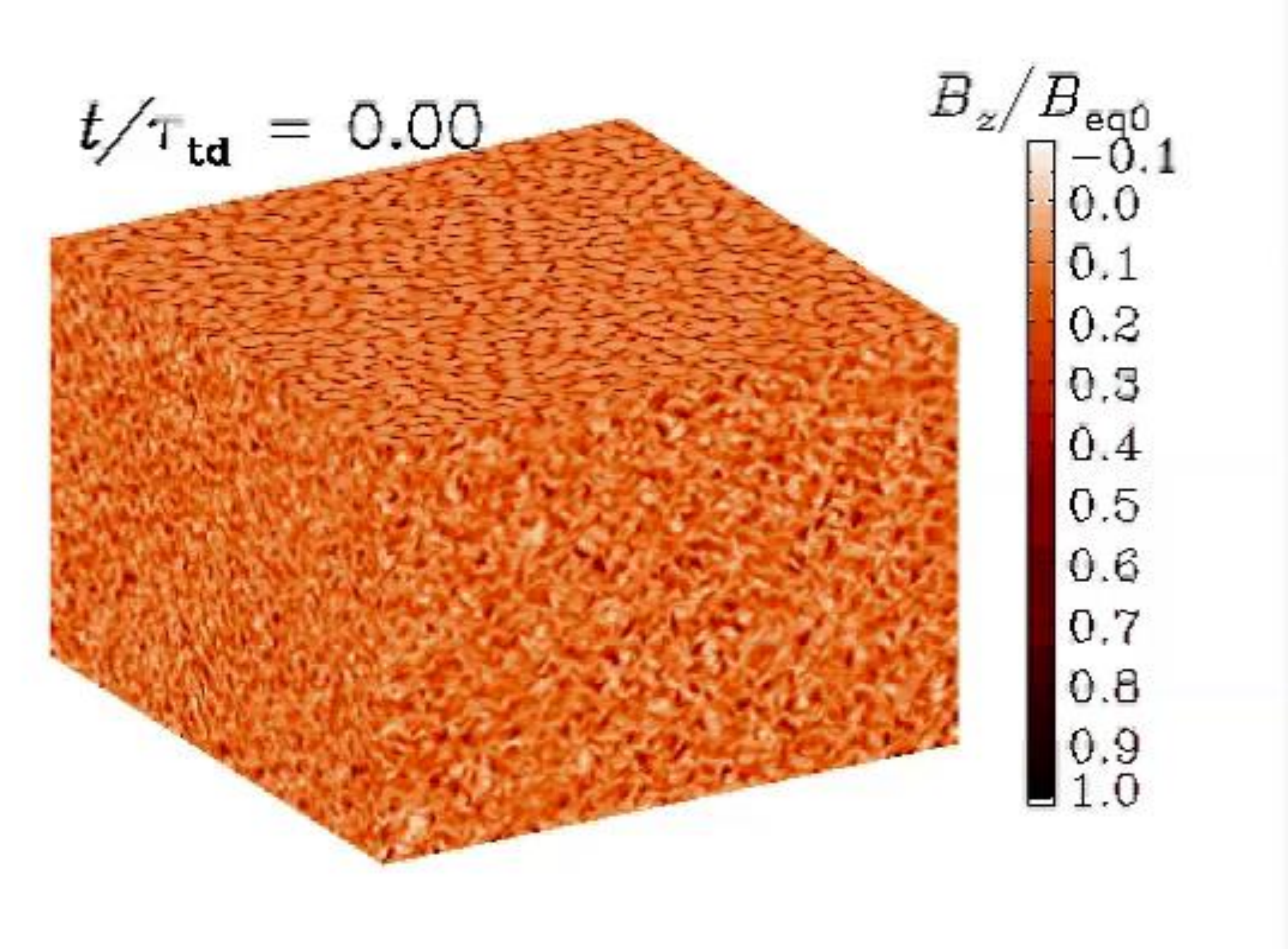

$$\mathrm{Pm} = \frac{\nu}{\eta} = \frac{1}{2}$$

$$\frac{\rho_{bot}}{\rho_{top}} = 535;$$

BOUNDARY CONDITIONS at the top and bottom:

1. stress-free conditions

$$\nabla_z U_x = \nabla_z U_y = 0$$

$$U_z = 0,$$

2. vertical field

$$B_x = B_y = 0,$$

Time-evolution of the Magnetic Spot

Brandenburg, Kleeorin, Rogachevskii, ApJL 776, L23 (2013)

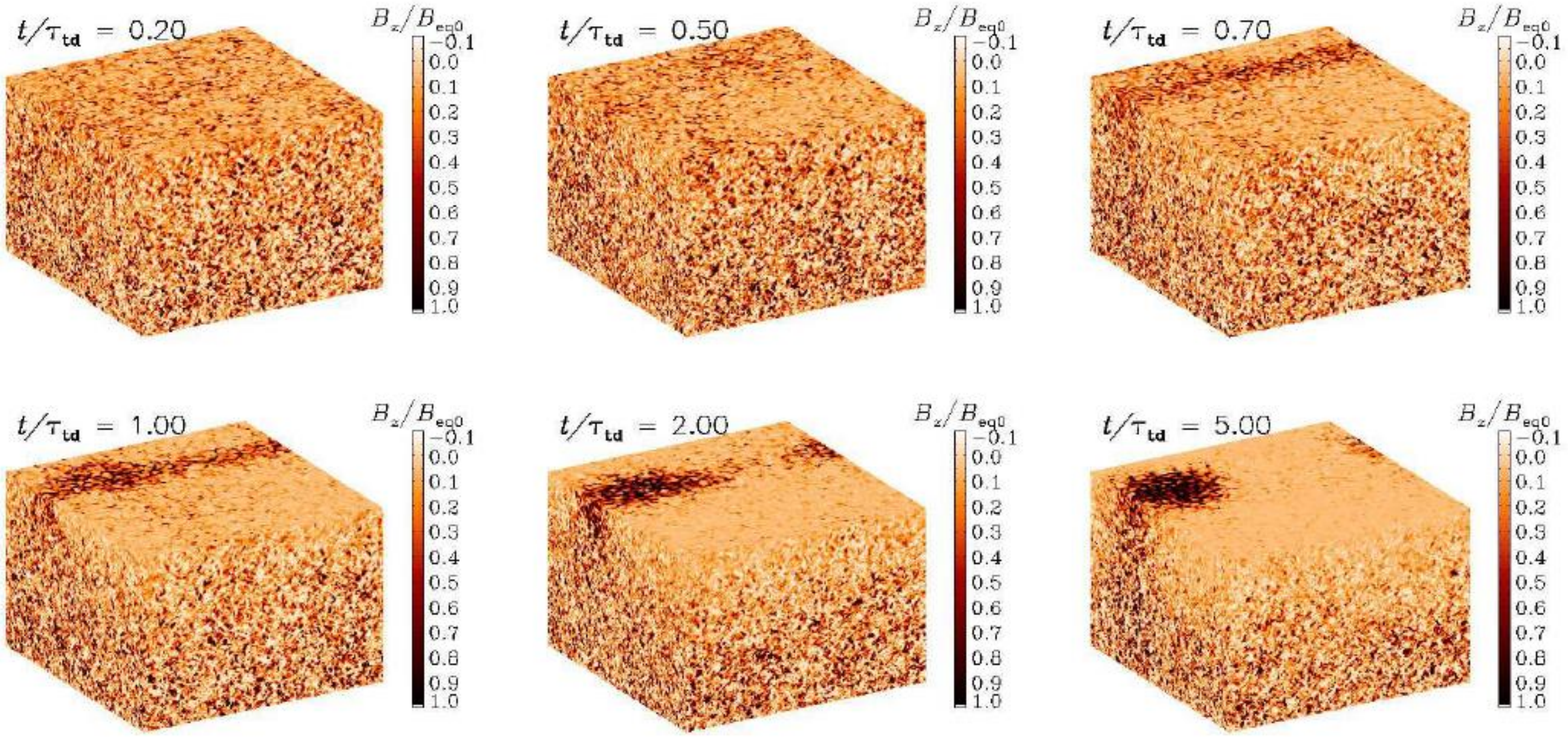

FIG. 1.— Evolution from a statistically uniform initial state toward a single spot for $B_{z0}/B_{eq0} = 0.02$. Here, B_z/B_{eq0} is shown on the periphery of the domain. Dark shades correspond to strong vertical fields. Time is in units of τ_{td}.

Structure of the Magnetic Spot

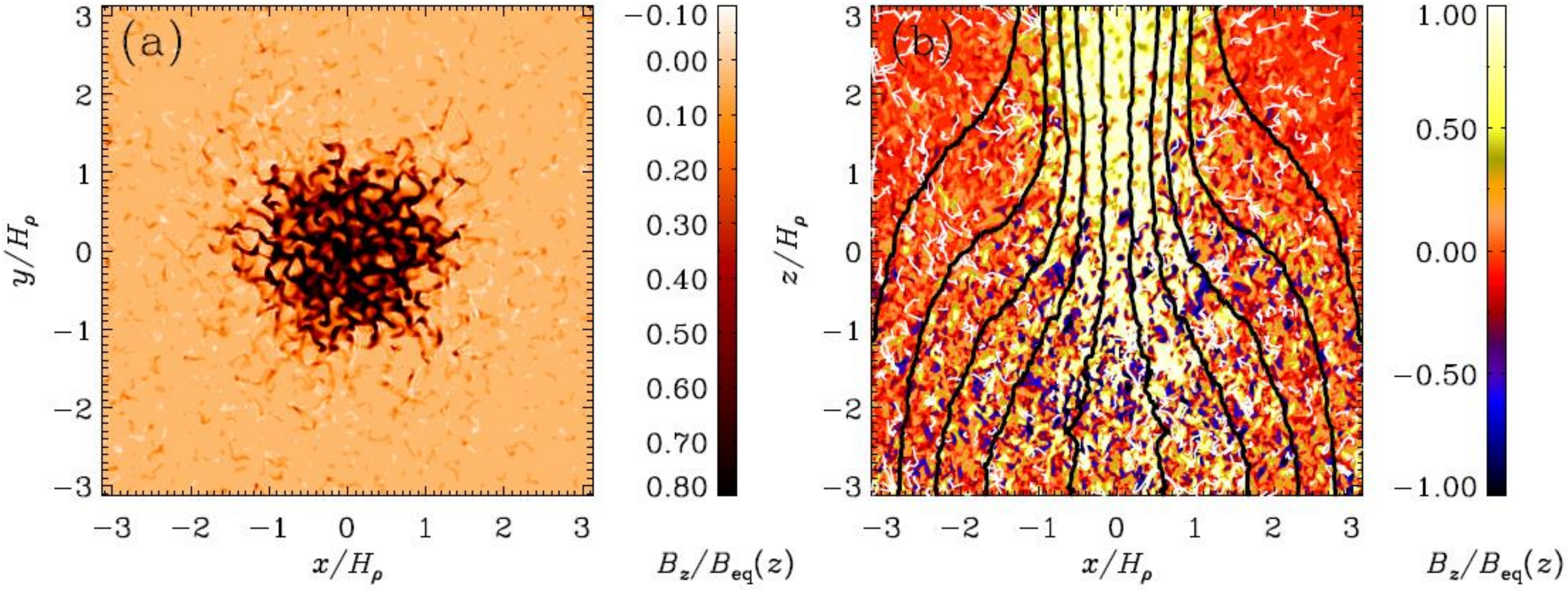

FIG. 3.— Cuts of $B_z/B_{\rm eq}(z)$ in the xy plane at the top boundary ($z/H_\rho = \pi$) and the xz plane through the middle of the spot at $y = 0$. In the xz cut, we also show magnetic field lines and flow vectors obtained by numerically averaging in azimuth around the spot.

Linear Phase of NEMPI

A. Brandenburg, N. Kleeorin and I. Rogachevskii, **Astrophys. J. Lett., 776, L23 (2013)**

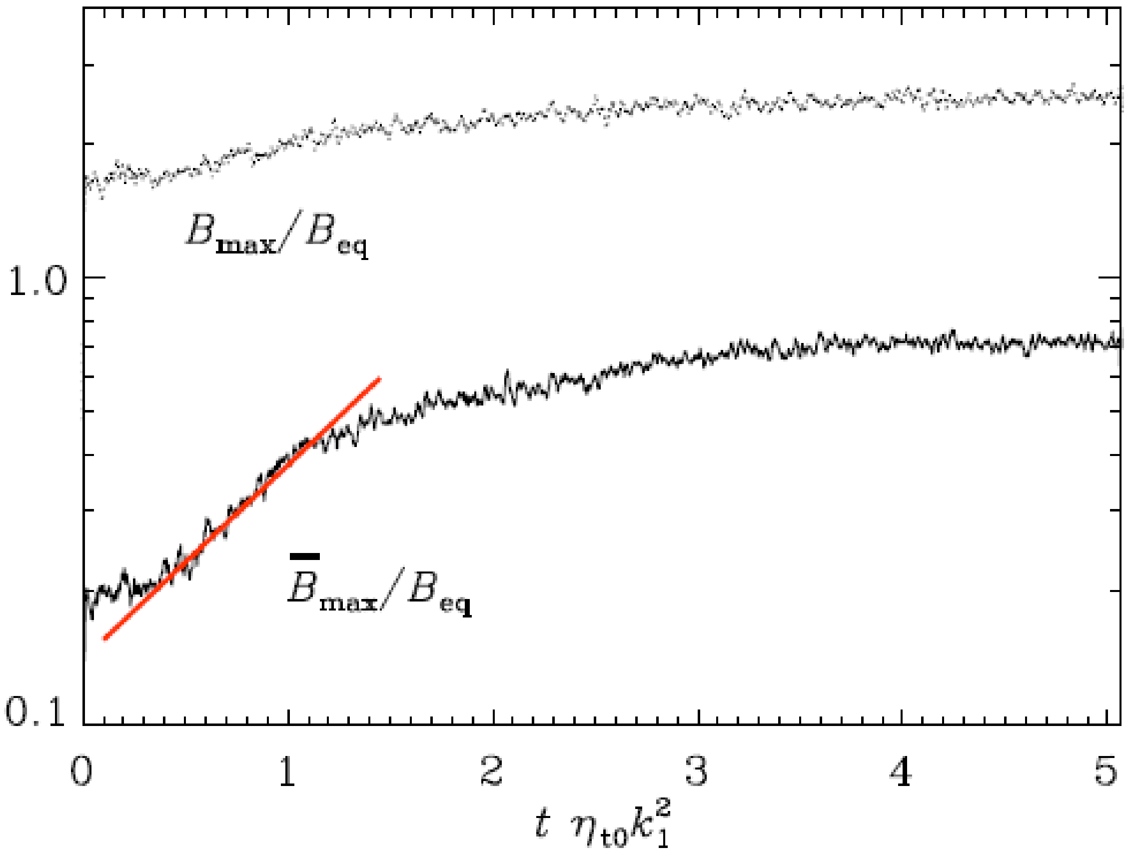

FIG. 2.— Growth of $\overline{B}_{\rm max}/B_{\rm eq}$ (solid line) and $B_{\rm max}/B_{\rm eq}$ (dotted line) at the top of the domain. The straight red line gives a fit to $\overline{B}_{\rm max}/B_{\rm eq}$ with a slope of unity corresponding to the growth rate $(\eta_{\rm t0}k_1^2)^{-1}$.

DNS in Two Forced Regions: Reconnection

Dh. Mitra, A. Brandenburg, N. Kleeorin, I. Rogachevskii, **MNRAS 445, 716 (2014).**

S. Jabbary, A. Brandenburg, Dh. Mitra, N. Kleeorin, I. Rogachevskii,
MNRAS 459, 4046 (2016).

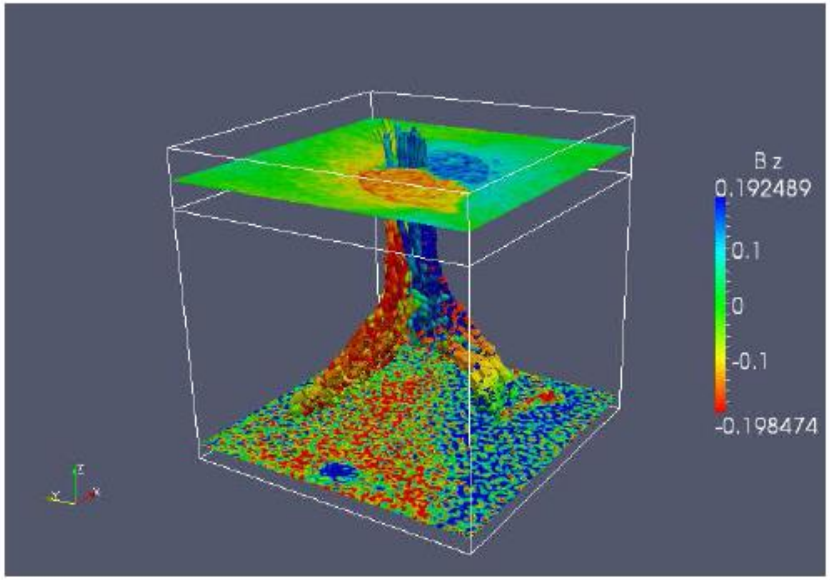

Figure 8. Magnetic field structure for Run A at time $t/\tau_{\rm td} \approx 1.2$. The z component of the magnetic field, B_z is plotted at $z/H_\rho = 3.$. The height up to which dynamo operates, $z_0/H_\rho = 2$, is also shown as a frame. Here magnetic field, B_z is not normalized, but in units of $\sqrt{\langle\rho(z=0)\rangle_{xy}}c_{\rm s}$. In the same units $B_{\rm eq}^0 \approx 0.1$.

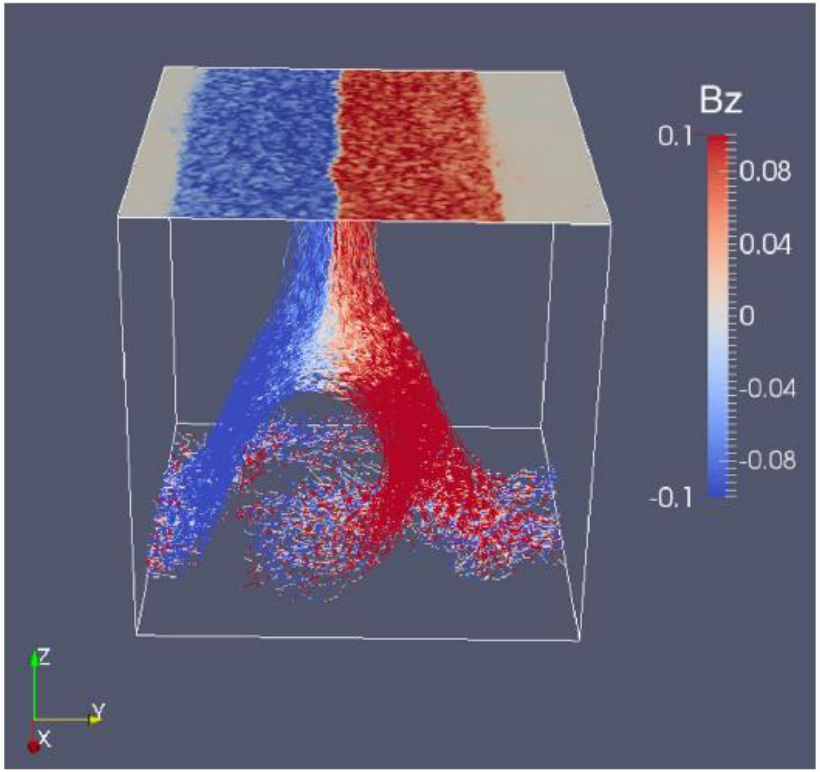

Figure 4. Three-dimensional visualization of vertical magnetic field, B_z at the surface (colour-coded) together with three-dimensional volume rendering of the vertical component of the magnetic field for Run RM1.

Oscillatory α^2 dynamo

S. Jabbary, A. Brandenburg, Dh. Mitra, N. Kleeorin, I. Rogachevskii,
MNRAS 459, 4046 (2016).

The dynamo operator is not self-adjoint because alpha vanishes only at one boundary, while it is non-zero at the other boundary. It has complex eigenvalues, and dynamo oscillatory.

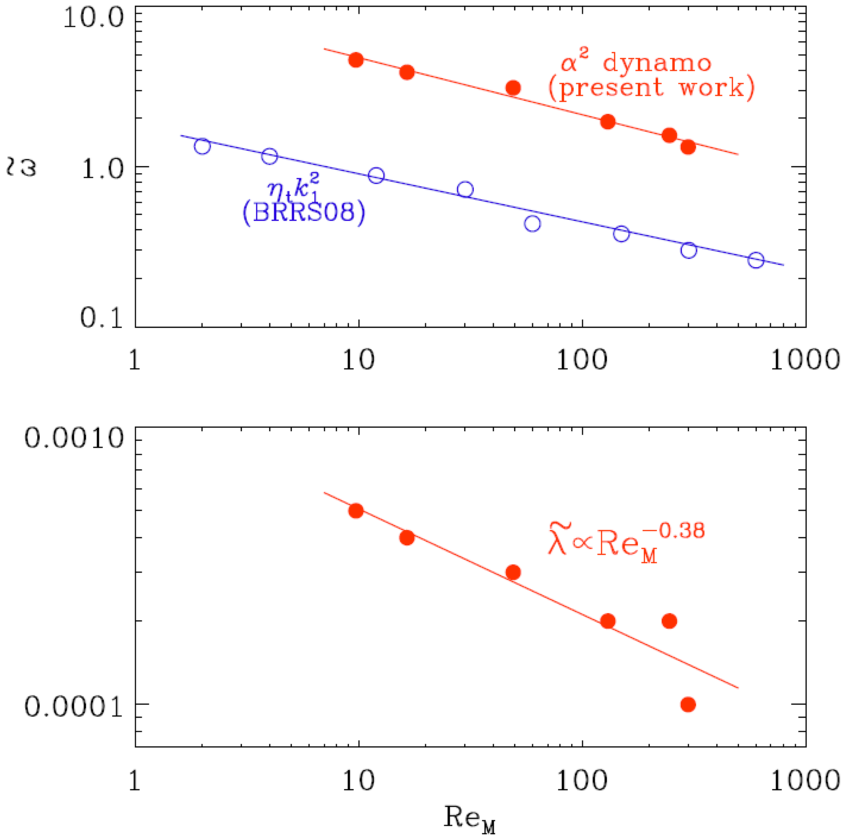

Figure 2. Upper panel: normalized dynamo frequency, $\tilde{\omega}$, as a function of Re_M. The solid lines show the best fit to our data points (red closed circles) and the data points of Brandenburg et al. (2008, blue open circles). Lower panel: normalized growth rate of dynamo, $\tilde{\lambda}$, as a function of Re_M. The solid line shows the best fit to our data points.

Formation of the Current Sheet and Reconnection

S. Jabbary, A. Brandenburg, Dh. Mitra, N. Kleeorin, I. Rogachevskii,
MNRAS 459, 4046 (2016).

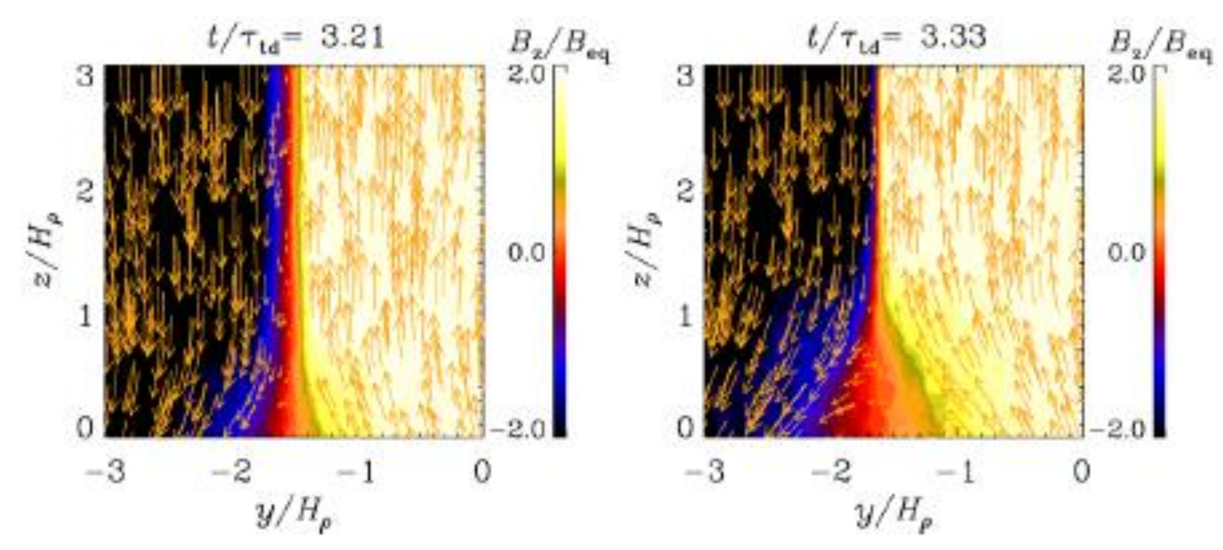

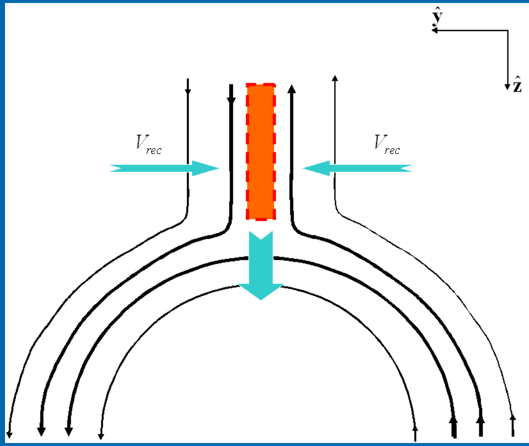

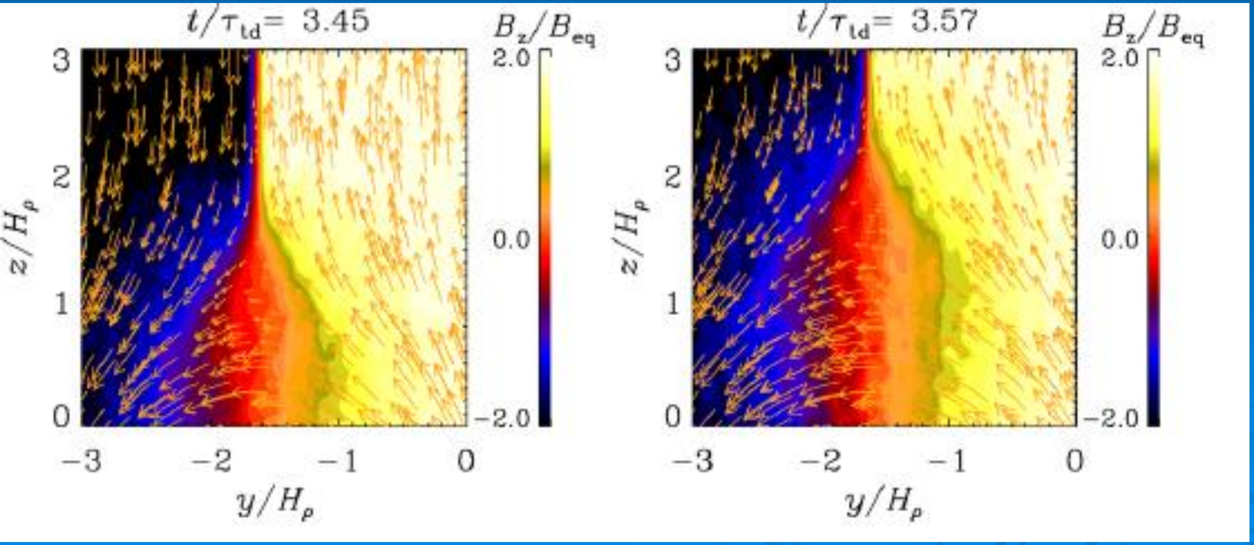

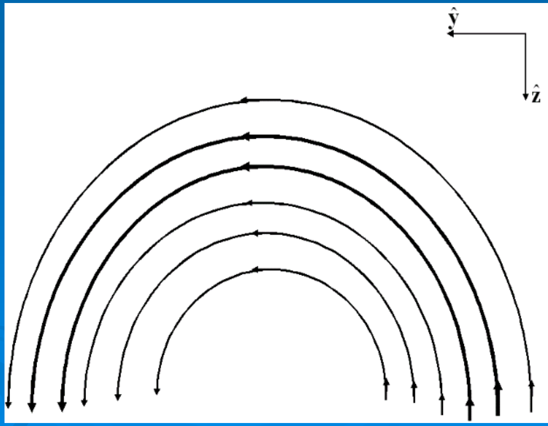

Reconnection Rate and Different Regimes

1. Sweet-Parker model (Parker (1957); Sweet (1969)):

$$V_{\rm rec} = V_{\rm A} S^{-1/2}$$

Lundquist number:

$$S = V_{\rm A} L/\eta$$

2. Lazarian-Vishniac (1999)

$$V_{\rm rec} \sim V_{\rm A} M_{\rm A}^2$$

Alfven Mach number:

$$M_{\rm A} = u_{\rm rms}/V_{\rm A}$$

3. Loureiro-Schekochihin-Cowley (2007)

$$V_{\rm rec} \sim 10^{-2} V_{\rm A}$$

Loureiro, N. F., Uzdensky, D. A., Schekochihin, A. A., Cowley, S. C., Yousef, T. A. 2009, MNRAS, 399, L146

Huang, Y.-M. & Bhattacharjee, A. 2010, Phys. Plasmas, 17, 062104

The Rate of Reconnection

The Ohm's law:

$$\eta J = E + U \times B$$

The rate of reconnection:

$$V_{\text{rec}} = \frac{|\langle E \rangle|}{|\langle B \rangle|} = \frac{|\eta \langle J \rangle - \langle U \times B \rangle|}{|\langle B \rangle|}.$$

Angular brackets imply averaging along z-direction.

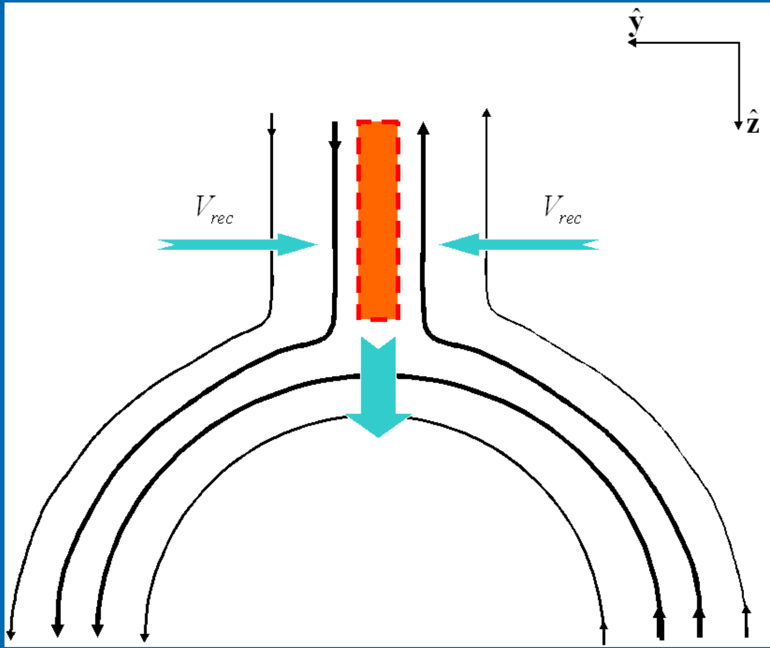

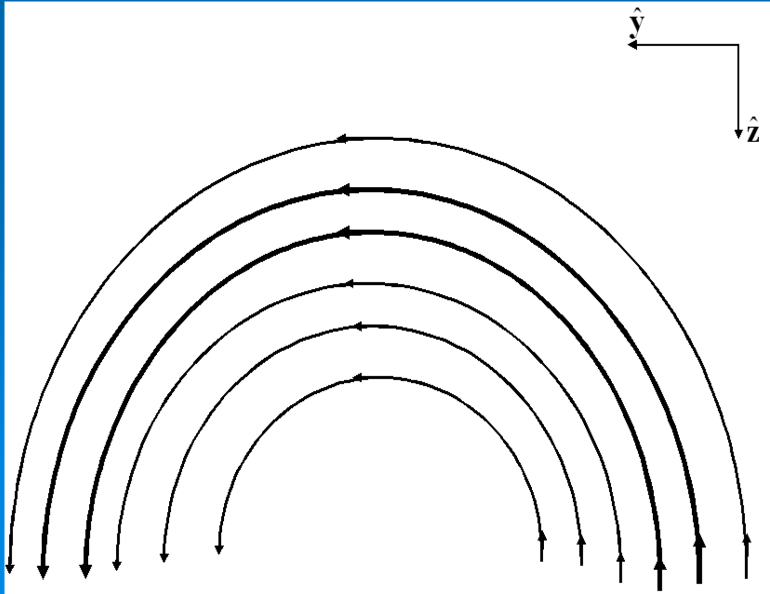

Reconnection Rate vs Lundqust Number

Loureiro-Schekochihin-Cowley (2007)

$$V_{\rm rec} \sim 10^{-2} V_{\rm A}$$

S. Jabbary, A. Brandenburg, Dh. Mitra, N. Kleeorin, I. Rogachevskii,
MNRAS 459, 4046 (2016).

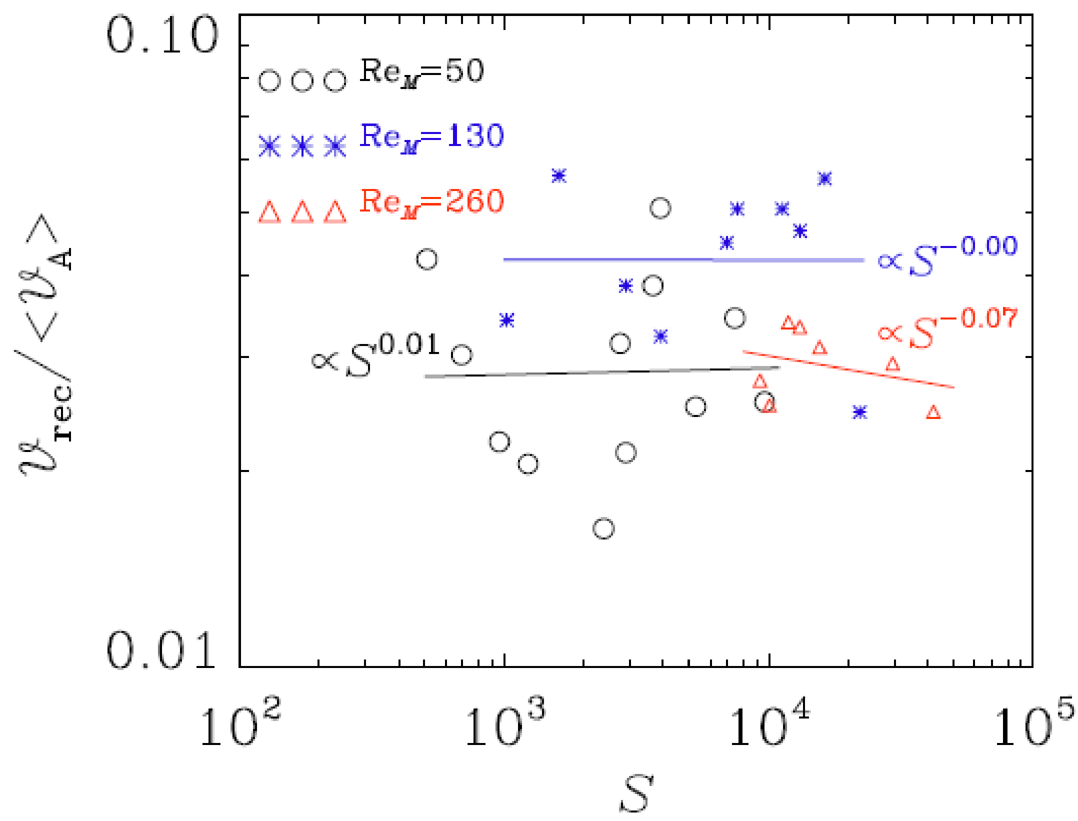

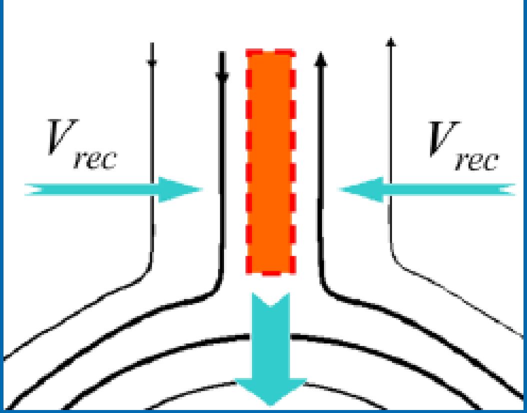

$$S = V_{\rm A} L/\eta$$

$$\mathrm{Re}_M = \frac{u_{\rm rms}}{\eta k_{\rm f}}, \quad \mathrm{Re} = \frac{u_{\rm rms}}{\nu k_{\rm f}}, \quad \mathrm{Pr}_M = \frac{\nu}{\eta},$$

ILES-Formation of Magnetic Flux Tubes (Vertical Imposed Weak Magnetic Field)

Brandenburg A., Gressel O., Jabbari S., Kleeorin N., and Rogachevskii I., Astron. Astrophys. 562, A53 (2014).

Boundary conditions are
1. Periodic in the horizontal directions,
2. Stress free on the upper and lower boundaries.
3. The magnetic field is assumed to be vertical.

The results from ILES are in good agreement with the DNS. This demonstrates that the mechanism causing magnetic flux concentrations by NEMPI is robust and not sensitive to details of the magnetic Reynolds numbers.

As the Mach number is increased, the magnetic structures become smaller.

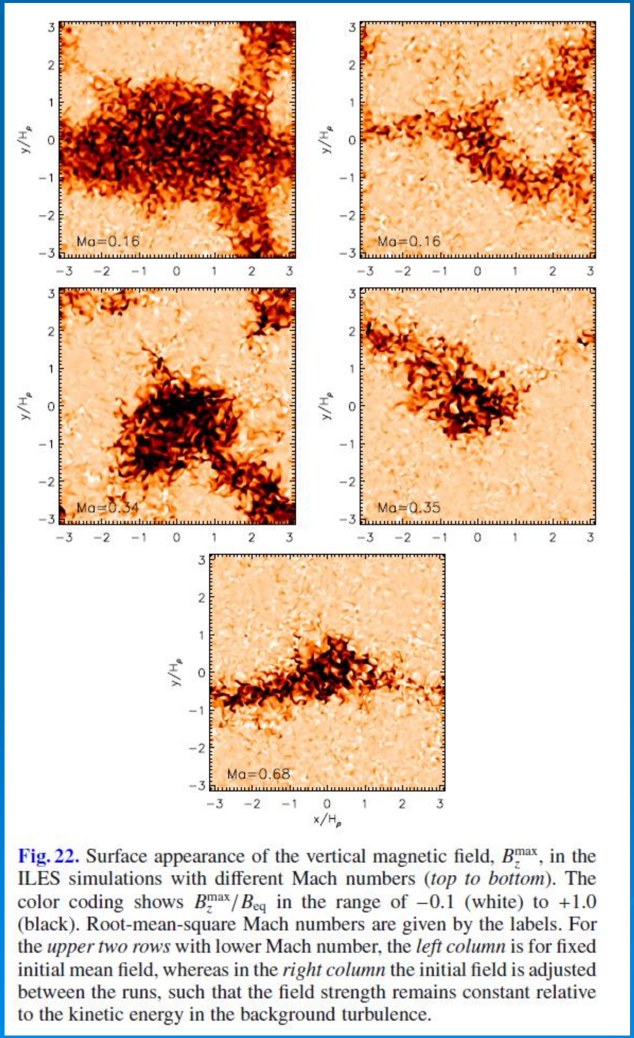

Fig. 22. Surface appearance of the vertical magnetic field, $B_z^{\max}$, in the ILES simulations with different Mach numbers (*top to bottom*). The color coding shows $B_z^{\max}/B_{\rm eq}$ in the range of -0.1 (white) to $+1.0$ (black). Root-mean-square Mach numbers are given by the labels. For the *upper two rows* with lower Mach number, the *left column* is for fixed initial mean field, whereas in the *right column* the initial field is adjusted between the runs, such that the field strength remains constant relative to the kinetic energy in the background turbulence.

$$\hat{\overline{B}} = \overline{B}/B_{\rm eq}$$

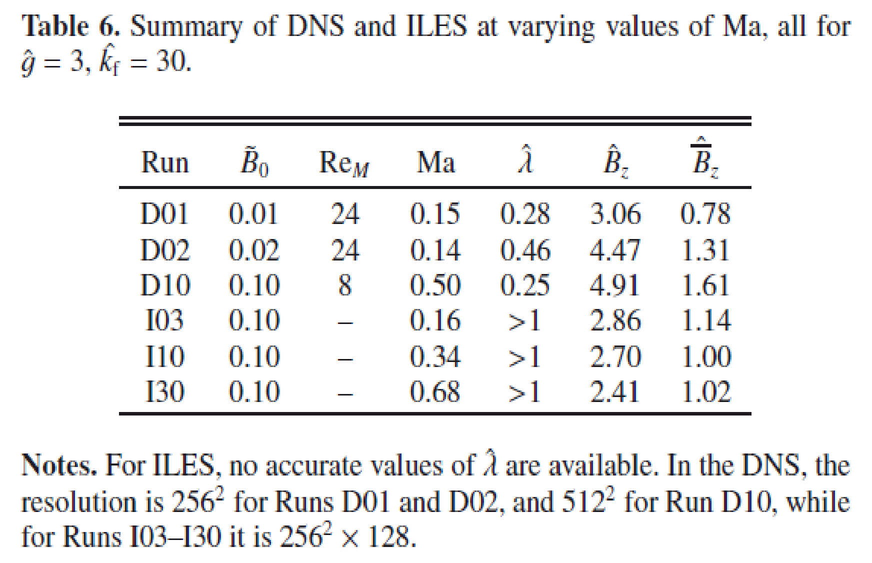

Table 6. Summary of DNS and ILES at varying values of Ma, all for $\hat{g} = 3$, $\hat{k}_{\rm f} = 30$.

Run	$\tilde{B}_0$	Re_M	Ma	$\hat{\lambda}$	$\hat{B}_z$	$\hat{\overline{B}}_z$
D01	0.01	24	0.15	0.28	3.06	0.78
D02	0.02	24	0.14	0.46	4.47	1.31
D10	0.10	8	0.50	0.25	4.91	1.61
I03	0.10	–	0.16	>1	2.86	1.14
I10	0.10	–	0.34	>1	2.70	1.00
I30	0.10	–	0.68	>1	2.41	1.02

Notes. For ILES, no accurate values of $\hat{\lambda}$ are available. In the DNS, the resolution is 256^2 for Runs D01 and D02, and 512^2 for Run D10, while for Runs I03–I30 it is $256^2 \times 128$.

ILES-Formation of Magnetic Flux Tubes (Vertical Imposed Weak Magnetic Field)

ILES are DNS without explicit physical dissipation coefficients (the dissipation scales are not resolved, but no turbulence parameterization model is used to represent the unresolved scales). The finite-volume code Nirvana is used.

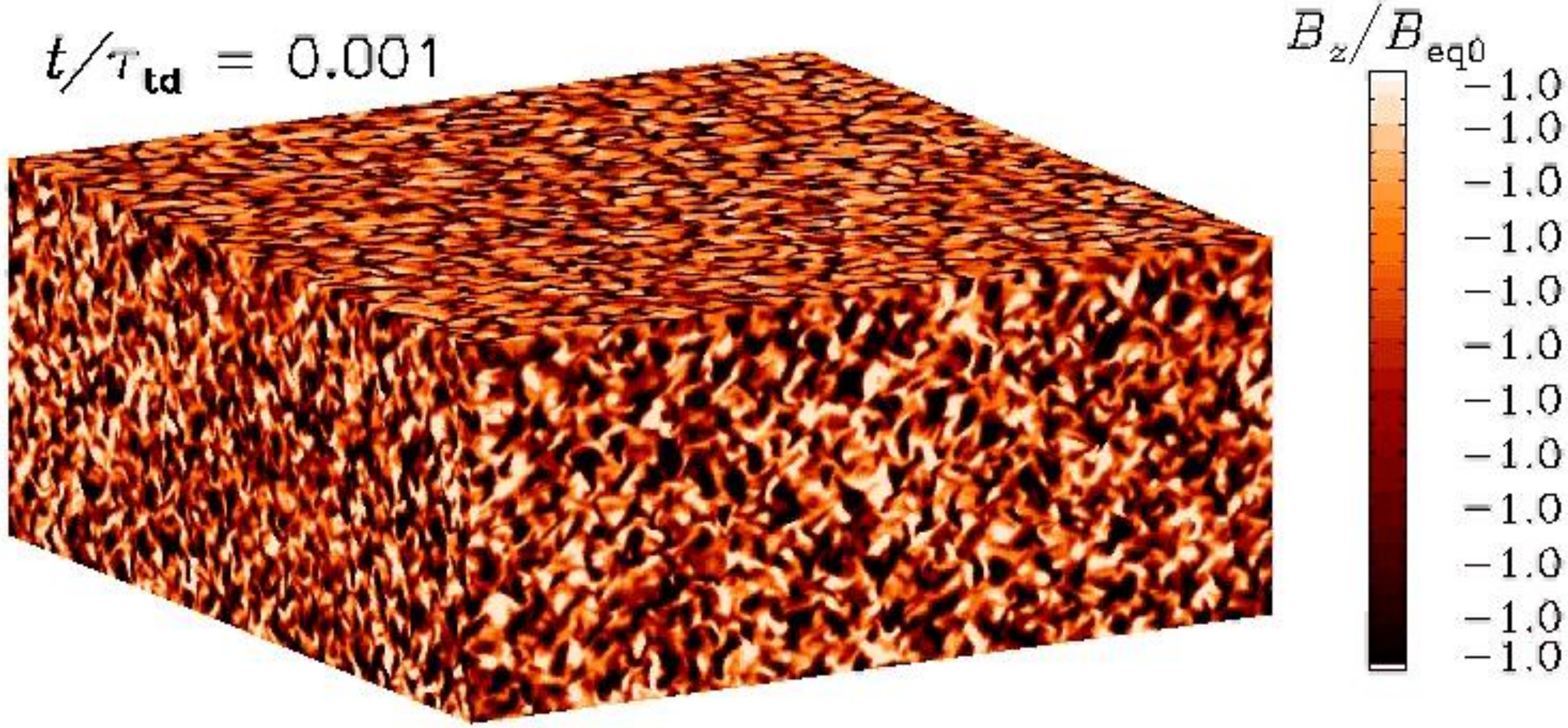

DNS and LES : 3D Turbulent Convection

P. Käpylä, A. Brandenburg, N. Kleeorin, M. Käpylä, I. Rogachevskii,
MNRAS, 422, 2465-2473 (2012); Astron. Astrophys. 588, A150 (2016).

$$\begin{aligned}
\frac{\partial \boldsymbol{A}}{\partial t} &= \boldsymbol{U} \times \boldsymbol{B} - \eta\mu_0 \boldsymbol{J}, \\
\frac{D \ln \rho}{Dt} &= -\boldsymbol{\nabla} \cdot \boldsymbol{U}, \\
\frac{D\boldsymbol{U}}{Dt} &= -\frac{1}{\rho}\boldsymbol{\nabla} p + \boldsymbol{g} + \frac{1}{\rho}\boldsymbol{J} \times \boldsymbol{B} + \frac{1}{\rho}\boldsymbol{\nabla} \cdot 2\nu\rho\mathbf{S}, \\
\frac{De}{Dt} &= -\frac{p}{\rho}\boldsymbol{\nabla} \cdot \boldsymbol{U} + \frac{1}{\rho}\boldsymbol{\nabla} \cdot K\boldsymbol{\nabla} T + 2\nu\mathbf{S}^2 + \frac{\mu_0\eta}{\rho}\boldsymbol{J}^2,
\end{aligned}$$

$$\boldsymbol{B} = \boldsymbol{B}_0 + \boldsymbol{\nabla} \times \boldsymbol{A}$$

$$\mathrm{Re} = \frac{u_{rms}\, d}{2\pi\, \nu} = 68 - 114,$$

$$\mathrm{Rm} = \frac{u_{rms}\, d}{2\pi\, \eta} = 25 - 55,$$

$$L_x = L_y = 5L_z = 5d; \quad (L_x = 10d) \qquad \frac{\rho_{bot}}{\rho_{top}} = 3 \times 10^3$$

the models that are 24 Mm deep.

BOUNDARY CONDITIONS:

$$U_z = 0, \quad \nabla_z U_x = \nabla_z U_y = 0$$

$$B_z \neq 0, \quad B_x = B_y = 0$$

BOUNDARY CONDITIONS:

1).The horizontal boundaries are periodic.
2). We keep the temperature fixed at the top and bottom boundaries.
3) For the velocity we apply impenetrable, stress-free conditions.
4). For the magnetic field we use vertical field conditions.

Effective Magnetic Pressure is Negative in DNS and LES with Turbulent Convection: but no NEMPI

P. Käpylä, A. Brandenburg, N. Kleeorin, M. Käpylä, I. Rogachevskii,
MNRAS, 422, 2465-2473 (2012); Astron. Astrophys. 588, A150 (2016).

$$\mathrm{F}^{\mathrm{eff}} = -\frac{1}{2}\nabla(1-q_p)\bar{\mathrm{B}}^2 + (\bar{\mathrm{B}}\cdot\nabla)(1-q_s)\bar{\mathrm{B}}$$

We perform horizontal averages which show a strong dependence on height.

We also perform time averaging in order to improve the statistics.

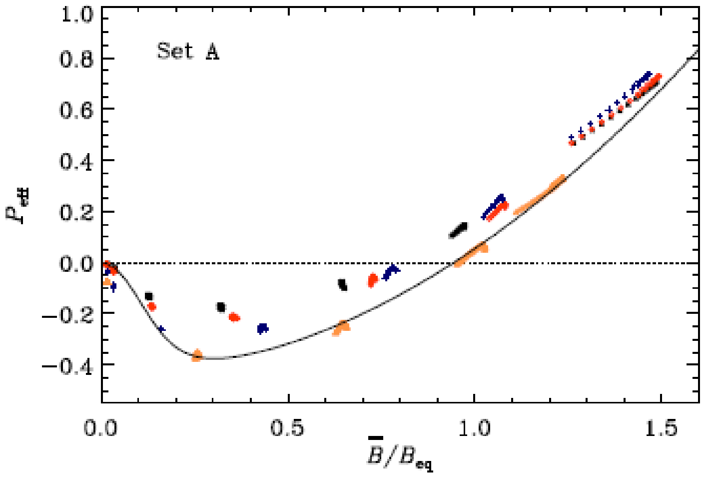

Figure 2. Effective magnetic pressure as a function of the mean magnetic field from weakly stratified Runs A1–A29 with an imposed horizontal field $\boldsymbol{B}_0 = B_0\hat{\boldsymbol{x}}$. The black stars, red diamonds, blue crosses, and yellow triangles denote simulations with Rm $\approx$ 10, 20, 50, and 70, respectively. We omit points near the boundaries at $z/d < 0.35$ and $z/d > 0.65$. The dashed and dotted lines correspond to approximate fits determined by Eq. (30), with $q_{p0} = 35$ and $B_p = 0.2B_{\rm eq}$, respectively.

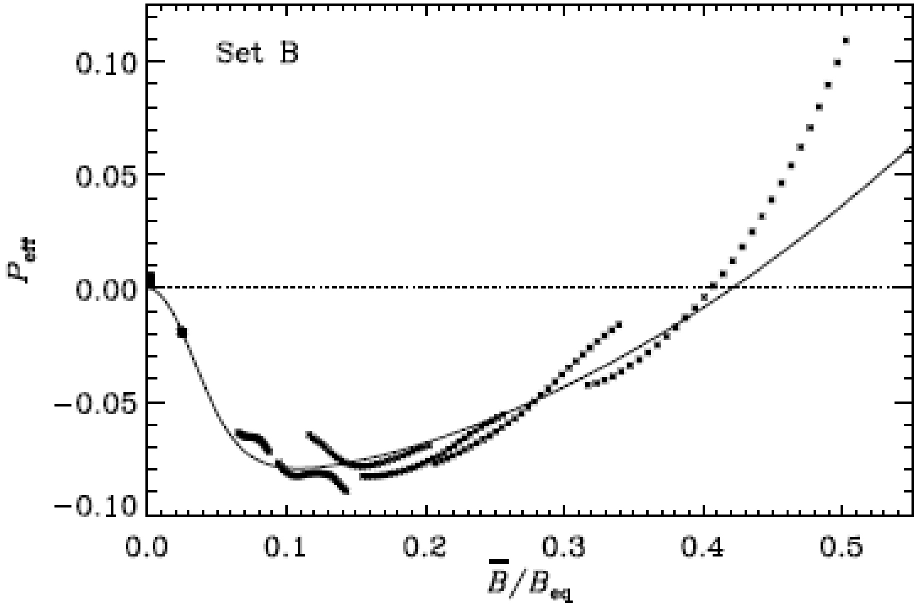

Figure 3. Same as Figure 2 but for Runs B1–B8 for Rm = 40–50. The solid line corresponds to a fit with $q_{\rm p0} = 70$ and $B_{\rm p} = 0.063B_{\rm eq}$

Effective Magnetic Pressure is Negative in DNS and LES with Turbulent Convection: but no NEMPI

. Käpylä, A. Brandenburg, N. Kleeorin, M. Käpylä, I. Rogachevskii, MNRAS, 422, 2465-2473 (2012); Astron. Astrophys. 588, A150 (2016).

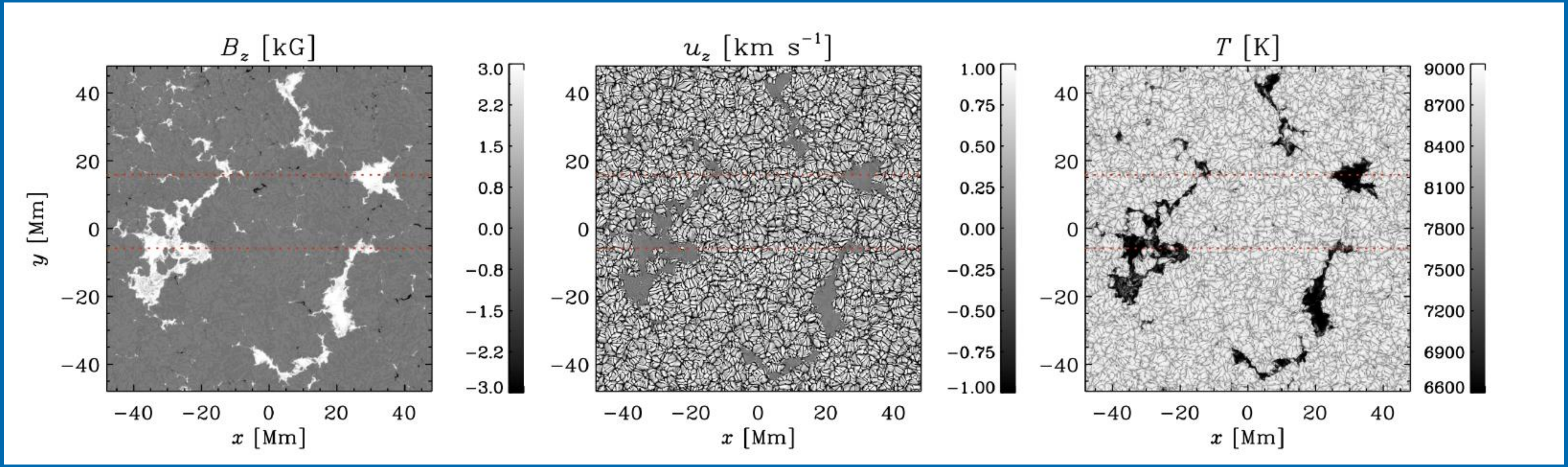

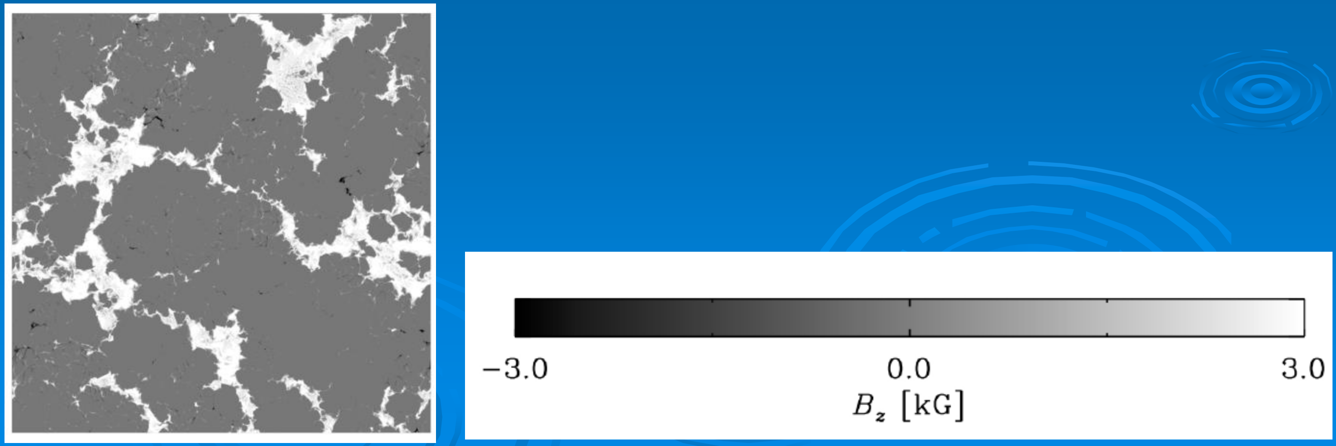

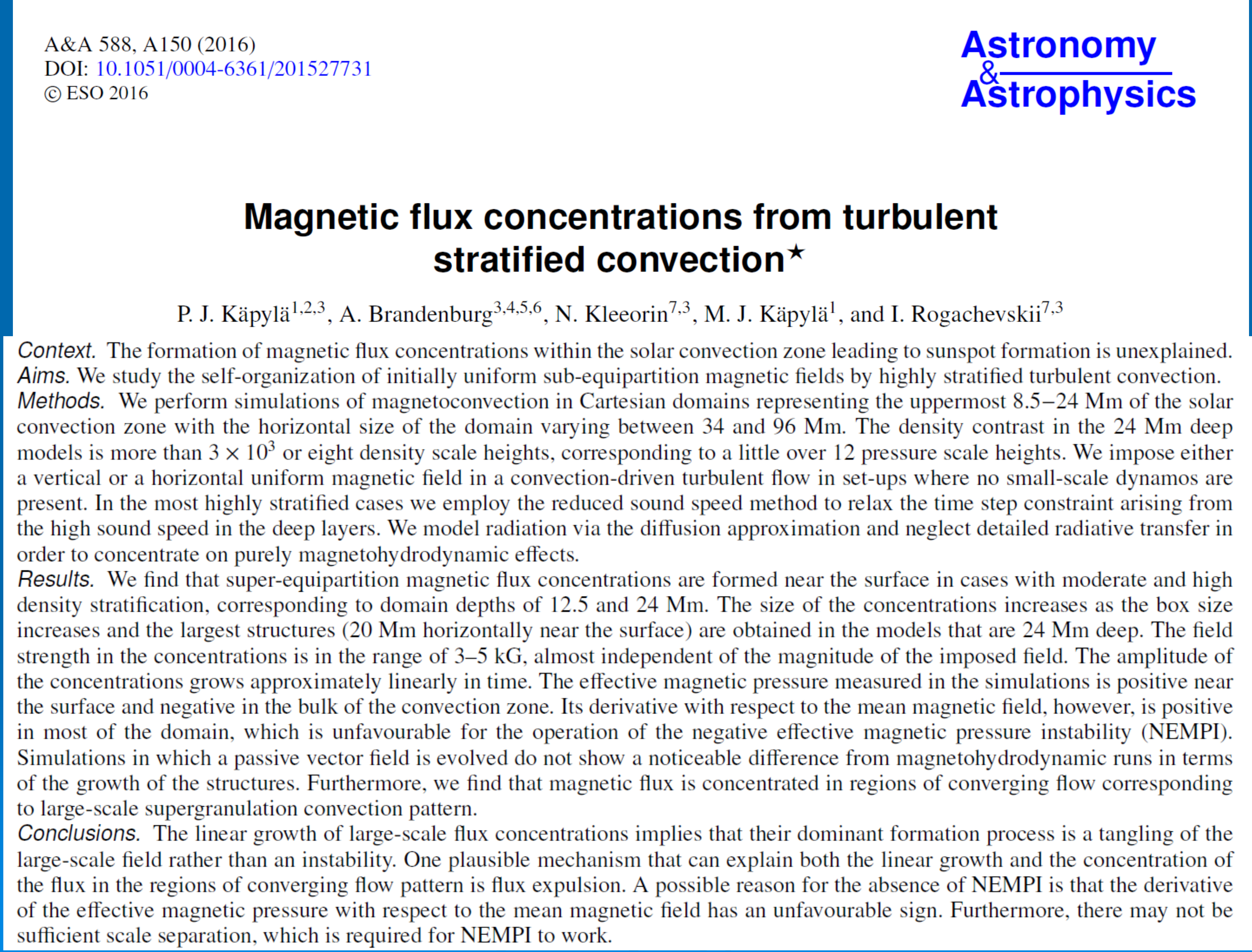

A&A 588, A150 (2016)
DOI: 10.1051/0004-6361/201527731

Astronomy
&
Astrophysics

Magnetic flux concentrations from turbulent stratified convection★

P. J. Käpylä[1,2,3], A. Brandenburg[3,4,5,6], N. Kleeorin[7,3], M. J. Käpylä[1], and I. Rogachevskii[7,3]

Context. The formation of magnetic flux concentrations within the solar convection zone leading to sunspot formation is unexplained.
Aims. We study the self-organization of initially uniform sub-equipartition magnetic fields by highly stratified turbulent convection.
Methods. We perform simulations of magnetoconvection in Cartesian domains representing the uppermost 8.5–24 Mm of the solar convection zone with the horizontal size of the domain varying between 34 and 96 Mm. The density contrast in the 24 Mm deep models is more than 3×10^3 or eight density scale heights, corresponding to a little over 12 pressure scale heights. We impose either a vertical or a horizontal uniform magnetic field in a convection-driven turbulent flow in set-ups where no small-scale dynamos are present. In the most highly stratified cases we employ the reduced sound speed method to relax the time step constraint arising from the high sound speed in the deep layers. We model radiation via the diffusion approximation and neglect detailed radiative transfer in order to concentrate on purely magnetohydrodynamic effects.
Results. We find that super-equipartition magnetic flux concentrations are formed near the surface in cases with moderate and high density stratification, corresponding to domain depths of 12.5 and 24 Mm. The size of the concentrations increases as the box size increases and the largest structures (20 Mm horizontally near the surface) are obtained in the models that are 24 Mm deep. The field strength in the concentrations is in the range of 3–5 kG, almost independent of the magnitude of the imposed field. The amplitude of the concentrations grows approximately linearly in time. The effective magnetic pressure measured in the simulations is positive near the surface and negative in the bulk of the convection zone. Its derivative with respect to the mean magnetic field, however, is positive in most of the domain, which is unfavourable for the operation of the negative effective magnetic pressure instability (NEMPI). Simulations in which a passive vector field is evolved do not show a noticeable difference from magnetohydrodynamic runs in terms of the growth of the structures. Furthermore, we find that magnetic flux is concentrated in regions of converging flow corresponding to large-scale supergranulation convection pattern.
Conclusions. The linear growth of large-scale flux concentrations implies that their dominant formation process is a tangling of the large-scale field rather than an instability. One plausible mechanism that can explain both the linear growth and the concentration of the flux in the regions of converging flow pattern is flux expulsion. A possible reason for the absence of NEMPI is that the derivative of the effective magnetic pressure with respect to the mean magnetic field has an unfavourable sign. Furthermore, there may not be sufficient scale separation, which is required for NEMPI to work.

Parameters (top of Solar Convective Zone)

In the upper part of the convective zone, at depth depth $H \sim 10^9$ **cm**,

the magnetic Reynolds number $\mathrm{Rm} \sim 3 \times 10^7$,

the maximum scale of turbulent motions $l_0 \sim 2.8 \times 10^8$ **cm**,

the characteristic turbulent velocity in the maximum scale l_0 of turbulent motions $u_0 \sim 10^4$ **cm s**$^{-1}$,

the turbulent magnetic diffusion $\eta_T \sim 10^{12}$ **cm**^{2} **s**$^{-1}$,

the equipartition mean magnetic field $\bar{B}_{\mathrm{eq}} = 700$ **G**.

the characteristic time of developing of the instability $T \sim 1.2$ **days**; the turbulent diffusion time $T_D \sim 12$ **days**; the critical magnetic field for the instability $\bar{B}_{\mathrm{cr}} = 0.03 \bar{B}_{\mathrm{eq}}$.

Realistic Simulations in Turbulent Convection

1. Stein, R. F., & Nordlund, °A. 2012, ApJ, 753, L13

The formation of bipolar regions has recently been found in realistic radiation-magnetohydrodynamics simulations of near-surface convection where 1 kG magnetic fields were inserted at the bottom of a 20 Mm deep box.

2. Cheung, M. C. M., Rempel, M., Title, A. M., & Sch¨ussler, M. 2010, ApJ, 233 ,720

Bipolar magnetic regions have previously been studied by advecting a semi-torus shaped twisted flux tube of 9 kG through the bottom boundary at 7.5 Mm depth of thermally relaxed convection.

3. Rempel, M. 2011, ApJ, 740, 15

Realistic numerical simulations of turbulent convection can find new properties of sunspots. These simulations have shown that a realistic, sunspot-like appearance of the magnetic field can be obtained when the field is kept fixed at the bottom of the domain.

All these studies emphasize the importance of radiative transfer.

Realistic Simulations in Turbulent Convection

4. Kitiashvili, I. N., Kosovichev, A. G., Wray, A. A., & Mansour, N. N. 2010, ApJ, 307 ,719.

Another radiative magnetohydrodynamics simulation with realistic physics also find spontaneous flux concentrations as a result of strongly converging flows, even though their domain is more shallow and without supergranulation.

5. Tao, L., Weiss, N. O., Brownjohn, D. P., & Proctor, M. R. E. 1998, ApJ, 496, L39.

This work might also be related to recent realistic simulations which showed that magneto-convection tends to segregate into magnetized and unmagnetized regions.

References: Theory

- **N. Kleeorin, I. Rogachevskii and A. Ruzmaikin,**
  Sov. Astron. Lett. 15, 274-277 (1989)
  Sov. Phys. JETP 70, 878-883 (1990)

- **N. Kleeorin and I. Rogachevskii,**
  Phys. Rev. E 50, 2716-2730 (1994)

- **N. Kleeorin, M. Mond and I. Rogachevskii,**
  Phys. Fluids B 5, 4128 -4134 (1993)
  Astron. Astrophys. 307, 293-309 (1996)

- **I. Rogachevskii and N. Kleeorin,**
  Phys. Rev. E 76, 056307 (2007)

References: DNS, LES, MFS

- A. Brandenburg, N. Kleeorin and I. Rogachevskii, Astron. Nachr. 331, 5-13 (2010); Astrophys. J. Lett., 776, L23 (2013);
- A. Brandenburg, K. Kemel, N. Kleeorin, Dh. Mitra, and I. Rogachevskii, Astrophys. J. Lett. 740, L50 (2011); Solar Phys. 280, 321-333 (2012); 287, 293-313 (2013);
- A. Brandenburg, K. Kemel, N. Kleeorin and I. Rogachevskii, Astrophys. J. 749, 179 (2012);
- P. Käpylä, A. Brandenburg, N. Kleeorin, M. Käpylä, I. Rogachevskii, MNRAS, 422, 2465-2473 (2012); Astron. Astrophys. 588, A150 (2016).
- J. Warnecke, I.R. Losada, A. Brandenburg, N. Kleeorin and I. Rogachevskii, Astrophys. J. Lett., 777, L37 (2013); Astron. Astrophys., 589, A125 (2016).
- I.R. Losada, A. Brandenburg, N. Kleeorin, I. Rogachevskii, Astron. Astrophys. 548, A49 (2012); 556, A83 (2013); 564, A2 (2014); 621, A61 (2019).
- S. Jabbari, A. Brandenburg, N. Kleeorin, Dh. Mitra, I. Rogachevskii, Astron. Astrophys. 556, A106 (2013); 562, A53 (2014); MNRAS 459, 4046-4056 (2016).
- Dh. Mitra, A. Brandenburg, N. Kleeorin, I. Rogachevskii, MNRAS 445, 716 (2014).
- Brandenburg A., Gressel O., Jabbari S., Kleeorin N., and Rogachevskii I., Astron. Astrophys. 562, A53 (2014).

THE END